The Stochastic Dynamics of Optomechanical Sensors for Atomic Force Microscopy

Stephen D. Epstein

Thesis submitted to the Faculty of the
Virginia Polytechnic Institute and State University
in partial fulfillment of the requirements for the degree of

Master of Science
in
Engineering Mechanics

Mark R. Paul, Chair
Saad A. Ragab
Shane D. Ross

July 15, 2013
Blacksburg, Virginia

Keywords: optomechanics, atomic force microscopy, noise spectrum

The Stochastic Dynamics of Optomechanical Sensors for Atomic Force Microscopy

Stephen D. Epstein

(ABSTRACT)

This work explores the stochastic dynamics and important diagnostics of a mechanical resonator (nanobeam) used in cavity optomechanical sensors for atomic force microscopy. Atomic force microscopy (AFM) is a tool to image surface topology down to the level of individual atoms. Conventional AFM has been an essential tool for micro and nanoscale studies in physics, chemistry, and biology. Cavity optomechanical sensors for AFM extend the utility of conventional AFM into a new regime of high sensitivity $k \approx 1\,\mathrm{N/m}$ and high frequency $f_0 \approx 10\,\mathrm{MHz}$. Cavity optomechanical sensors for AFM are unique because they use near field optics to transduce the position of a nanobeam. The nanobeam is not able to be transduced by more conventional AFM techniques, such as laser interferometry, because the nanobeam is smaller than the spot size of the laser.

This work determines the noise spectrum G of a nanobeam in water and in air. Also important diagnostics of the nanobeam are determined in air and in water. These important diagnostics include the quality factor Q and natural frequency in fluid ω_f. It is found that the nanobeam is overdamped in water. However, the nanobeam is underdamped in air and has quality factor of $Q \approx 4$. The noise spectrum is determined from deterministic numerical calculations and the Fluctuation-Dissipation Theorem. This is possible because the same molecular processes, Brownian motion, cause both the fluctuations of the nanobeam and the dissipation of the nanobeam.

Acknowledgments

First, I would like to thank my advisor for his support and guidance. His relentless pursuit of physical insights encouraged my scientific curiosity and his patient efforts raised the standards of my work. I would also like to thank my family, friends, and girlfriend for their unwavering support and encouragement.

Contents

List of Figures

List of Tables

Nomenclature

α	Eigenvalue
a	Positive optical mode frequency
B	Computation time per time step [min/step]
χ	Mechanical susceptibility
c	Speed of light in vacuum [m/s]
δ	Dirac delta function
δ_0	Stokes length evaluated at the natural frequency in vacuum [m]
δ_{rs}	Kronecker delta function
$\vec{\delta}$	Local computational coordinates
Δt	Time step [s]
$\vec{d}$	Displacement of the local computation coordinates [m]
$\vec{d_f}$	Fluid displacement on the fluid solid interfaces [m]
$\vec{d_s}$	Solid displacement on the fluid solid interfaces [m]
$\boldsymbol{e}_f$	Rate of strain tensor [1/s]
$\boldsymbol{e}_s$	Stretching tensor
E	Young's Modulus [N/m^2]
E_{tot}	Total energy [J]
f_0	Natural frequency in vacuum [Hz]
F	Applied force [N]

F_0 Magnitude of the applied force [N]

F_L Langevin force [N]

F_{RP} Radiation pressure force [N]

γ Power dissipation rate [rad/s]

Γ Hydrodynamic loading function

G Noise spectrum of the stochastic tip fluctuations [m^2/Hz]

h Height of the nanobeam [m]

I Second moment of area [m^4]

κ Fluid bulk modulus [Pa]

k Stiffness [N/m]

k_B Boltzmann constant [J]

Kn Knudsen number

λ Mean free path [m]

λ_f Second coefficient of viscosity [Pa s]

λ_s, μ_s Lamé constants [Pa]

L Length of the cantilever [m]

L^* Characteristic length [m]

m Mass per unit length [kg/m]

$\max \Delta x$ Maximum element length [m]

$\min \Delta x$ Minimum element length [m]

μ_f Dynamic fluid viscosity [Pa s]

ν Poisson's ratio

n Index of refraction

$\vec{n}$ Outward pointing normal

N Total number of elements

ω_0	Natural radial frequency in vacuum [rad/s]
ω_f	Natural frequency in fluid [rad/s]
ω_m	Natural frequency of mechanical resonator [rad/s]
$\tilde{\omega}$	Reduced frequency
P	Local pressure [Pa]
Q	Quality factor
Q_m	Quality factor of mechanical resonator
ρ_0	Reference density [kg/m^3]
ρ_f	Fluid density [kg/m^3]
ρ_s	Solid density [kg/m^3]
R	Frequency based Reynolds number
R_0	Frequency parameter evaluated at the natural frequency
Re	Velocity based Reynolds number
$\boldsymbol{\sigma}_s$	Solid Stress tensor [Pa]
s	Launched optical mode
s_g	Gap between the nanobeam and the microdisk [m]
s_w	Separation between the nanobeam and the walls that bound the fluid [m]
S_E	Sum of square error
SHO	Simple harmonic oscillator
τ_0	Intrinsic cavity loss
τ_{ex}	Power coupling into outgoing modes
t	Time [s]
t_{rt}	Round trip time [s]
T	Temperature [K]
T_0	Mass loading parameter

T^* Characteristic time [s]

U^* Characteristic velocity [m/s]

$\vec{v}$ Fluid velocity vector [m/s]

$\vec{V}_p$ Probe Velocity [m/s]

w Width of the nanobeam [m]

y Spontaneous fluctuations of the tip displacement [m]

Y The y component of the tip displacement [m]

Y_1 Displacement of an underdamped simpler harmonic oscillator [m]

Y_2 Displacement of an overdamped simpler harmonic oscillator [m]

$\vec{Y}$ Cantilever displacement vector [m]

$\langle y(0)y(t)\rangle$ Autocorrelation of the stochastic tip fluctuations [m^2]

ζ Nondimensional refraction parameter

Chapter 1

Introduction

The introduction to this work first describes conventional atomic force microscopy (AFM) and motivates the development of cavity optomechanical sensors for AFM. Then, the setup and operation of cavity optomechanical sensors for AFM is described. Finally, the contribution of this work is provided.

The atomic force microscope revolutionized surface science by providing topographical mappings of semiconductors, polymers, carbon nanotubes, and biological cells with atomic precision [26,27,37,38]. AFM relies on the ability to accurately detect the position of micro and nanoscale cantilevers. An example of a technique used to determine the position of an AFM cantilever is laser interferometry, which is illustrated in Figure 1.1. Laser interferometry consists of a laser that is reflected off the back side of a cantilever and a quadrant photodiode that measures the angle of reflection. The tip displacement is then inferred from this change in the angle of reflection.

Laser interferometry is a well established technique and can accurately detect the position of microscale cantilevers. However, it is unable to accurately detect the position of nanoscale cantilevers (nanobeams) that are smaller than the spot size of the laser. It is desired to use nanobeams in AFM because decreasing the size of the cantilever increases the frequency, while maintaining a high level of sensitivity.

The cantilever's frequency and sensitivity are important characteristics of an AFM. A high frequency is needed to measure interactions that occur on a small timescale. Many important application occur at small time scales. For example, some protein motions and deformations occur on a timescale of a few femtoseconds [6]. Also a high sensitivity is needed to measure soft samples, such as biological cells.

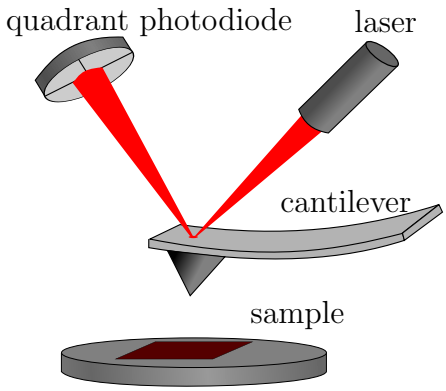

Figure 1.1: A typical laser interferometry setup consists of a laser, a quadrant photodiode, and a cantilever. A laser is reflected off the back side of the cantilever so the beam impacts the quadrant photodiode. The quadrant photodiode detects the change in angle of the cantilever and the tip displacement is then inferred from this change in angle.

In order to reap the befits of using nanobeams in AFM a new method of determining the position of nanobeams was needed. Cavity optomechanical sensors for AFM is a method that was recently developed to determine the position of nanobeams [34]. The nanobeams used in cavity optomechanical sensors for AFM are able to achieve over one hundred times higher acquisition rate than conventional AFM, while maintaining a high level of sensitivity as shown in Table 1.1.

	cantilever	nanobeam
f_0 [kHz]	10 - 1,100	200 - 110,000
k [N/m]	0.1 - 300	0.1 - 300
Q	40 - 1,000	5-100

Table 1.1: Typical properties of the cantilevers used in conventional AFM are compared with the properties of the nanobeams used in cavity optomechanical sensors for AFM. The natural frequency in vacuum f_0, which is approximately equal to the resonant frequency in air; the quality factor in air Q, and the stiffness k are compared [18, 21, 34].

A cavity optomechanical sensor for AFM consists of a nanobeam in close proximity to an optical resonator. A schematic of a cavity optomechanical sensor for AFM is provided in Figure 3.1. The nanobeam is anchored to the support structure on four faces and moves in plane with the microdisk. The nanobeam curves around the microdisk so that it interacts with a large portion of the circumference of the microdisk and it smoothly curves away from the microdisk to avoid abrupt transitions and thus limits scattering loss [34].

The optical setup consists of laser light that is sent through a waveguide to a photodetector. The waveguide couples to a microdisk optical resonator, which supports whispering gallery

modes. The light of the whispering gallery mode is guided around the circumference of the microdisk through total internal reflection. One of the first explorations of whispering gallery modes occurred at St Paul's Cathedral. Whispers (sound waves) could be heard on the other side of the dome at St Paul's Cathedral, but the secret messages were unable to be heard in the middle of the dome [28]. One of the amazing aspects of microdisk optical resonators is that the quality factor Q of the whispering gallery modes can be $Q \approx 10^5$ [34]. It is also important to note that even though the light is guided through total internal reflection, not all the power is carried inside the microdisk. Power is carried outside the microdisk in an evanescent wave. An evanescent wave decays exponentially and ensures the tangential components of the electric and magnetic fields are continuous at the boundaries of the microdisk [16].

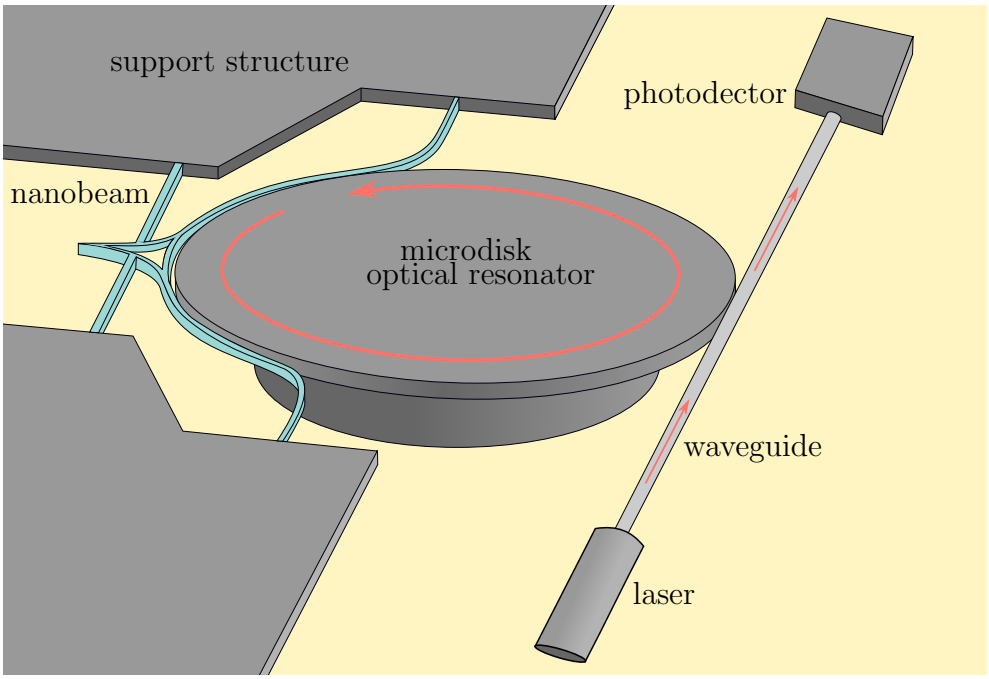

Figure 1.2: The set-up of an optomechanical sensor for atomic force microscopy. A waveguide is coupled to a whispering gallery mode microdisk optical resonator. The nanobeam wraps around the microdisk and interacts with the evanescent wave of the microdisk [34].

The interaction between the nanobeam and the optics occurs through the evanescent wave. A displacement of the nanobeam causes a shift in the resonant frequency of the optical mode. The shift in the optical mode causes an amplitude and phase shift in the outgoing optical mode, which is detected by the photodetector. The shift in the optical mode allows for the position of the nanobeam to be inferred.

Although the nanobeams used in cavity optomechanical sensors for AFM have a high natural frequency and high sensitivity in vacuum, their stochastic dynamics and properties in fluid

are largely unknown. The stochastic dynamics and properties of the nanobeam in fluid are important because many biological and chemical applications of AFM occur in water and in air at atmospheric pressure.

This work explores the stochastic dynamics of a nanobeam used in cavity optomechanical sensors for AFM in water and in air at atmospheric pressure. Understanding the stochastic dynamics is important for metrology because the inherent thermal noise of an experimental system sets the ultimate sensitivity of a particular measurement [26]. Also the stochastic dynamics can be used to determine the stiffness of the nanobeam [31].

A thermodynamic approach is used to determine the stochastic dynamics of a nanobeam used in optomechanical sensors for AFM. A thermodynamic approach uses deterministic numerical calculations and the Fluctuation-Dissipation Theorem to calculate the autocorrelation of the fluctuations of the nanobeam's displacement from equilibrium. Then the noise spectrum G is determined from the autocorrelation. The steps of the thermodynamic approach used are [10, 26]:

1. Apply a step force to the nanobeam in the distant past;
2. Remove the step force and record the tip displacement of the nanobeam as it relaxes back to equilibrium;
3. Use the Fluctuation-Dissipation Theorem to determine the auto-correlation of the fluctuations from equilibrium; and
4. Use the Wiener-Khinchin Theorem to determine the noise spectrum G.

This work also explores the nanobeam's natural frequency ω_f and quality factor Q in water and in air. The nanobeam is found to be overdamped in water and underdamped in air. Also the natural frequency of the nanobeam in air ω_f is found to be nearly the same as the natural frequency of the nanobeam in vacuum ω_0.

The main body of this work is divided into four chapters. First, Fundamentals describes how optomechanical interactions can be modeled, provides relevant results from statistical mechanics, and describes how the nanobeam and surrounding fluid is modeled. Second, Numeric Modeling describes the computational parameters used in creating the finite element model of the nanobeam and the surrounding fluid. Third, Code Validation compares the numeric noise spectrum of a cantilever to the analytic noise spectrum of the cantilever in order to validate the numerical setup and procedure. Lastly, Results provides the noise spectrum G, quality factor Q, and other important diagnostics of the nanobeam in water and then in air.

Chapter 2

Fundamentals

2.1 Optomechanical Systems

Optomechanical systems consist of an optical resonator coupled with a mechanical resonator. In many optomechanical systems the optical resonator acts as the mechanical resonator as well. The mechanism of optomechanics can be understood by examining the Fabry-Pérot resonator illustrated in Figure 2.1. The Fabry-Pérot resonator consists of an optical cavity between two mirrors. One of the mirrors is free to oscillate, while the other is fixed. Incident optical power that is resonant with a cavity mode creates a large circulating power within the cavity. This circulating power exerts a radiation pressure on the harmonically bounded mirror. The mirror's motion results in a new optical round trip condition and thus modifies the resonant frequency of the cavity. The coupling is non-linear and can manifest itself as hysteric behavior [19].

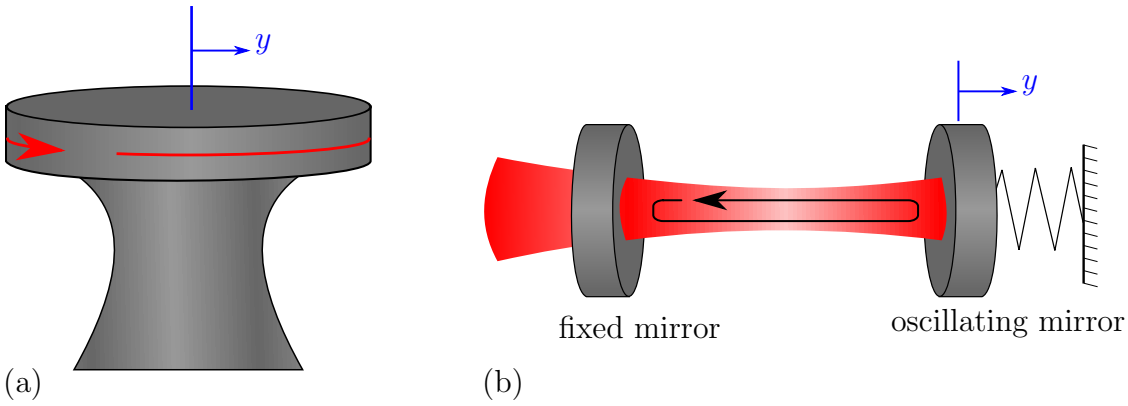

Figure 2.1: (a) A microdisk optical resonator consists of a microdisk with a refractive index n. The light is guided inside the microdisk by total internal reflection. The radiation pressure on the walls of the microdisk causes it to exhibit a radial breathing mode. (b) A Fabry-Pérot optical resonator consists of a semitransparent mirror and a harmonically bounded mirror. The radiation pressure causes the harmonically bounded mirror to vibrate, which is analogous to the breathing mode of (a).

The coupling between the mechanical and optical modes can be modeled as a set of two coupled ordinary differential equations [19]

$$\frac{da}{dt} = i\Delta a - \left(\frac{1}{2\tau_0} + \frac{1}{2\tau_{ex}}\right) a + i\sqrt{\frac{1}{\tau_{ex}}} s \tag{2.1}$$

$$\frac{d^2Y}{dt^2} + \frac{\omega_m}{2Q_m}\frac{dY}{dt} + \omega_m^2 Y = \frac{F_{RP}(t)}{m_{\text{eff}}} + \frac{F_L}{m_{\text{eff}}} = \frac{\zeta}{cm_{\text{eff}}}\frac{|a|^2}{t_{rt}} + \frac{F_L}{m_{\text{eff}}}. \tag{2.2}$$

Equation (2.1) governs the optical field where a is the positive mode frequency normalized so that $|a|^2$ is the stored cavity energy, $i = \sqrt{-1}$, Y is the displacement of the mirror and $|s|^2$ is the launched input power. Equation (2.1) is the result of a perturbation expansion that reduces the second order equation for the optical field to a first order equation [16]. The perturbation expansion relies on the high quality factor of the resonator, which can be $Q \approx 10^5$ for the microdisk optical resonators used in optomechanical sensors for AFM [34]. $\Delta = \omega - \omega_0(Y)$ accounts for the detuning of the pump laser with respect to the cavity resonant frequency. The optical field decays with a rate

$$\frac{1}{\tau} = \left(\frac{1}{2\tau_0} + \frac{1}{2\tau_{ex}}\right) \tag{2.3}$$

where $1/\tau_{ex}$ is the power coupling rate into outgoing modes. The intrinsic cavity loss rate is described by $1/\tau_0$. Equation (2.2) governs the mechanical degree of freedom Y, which is assumed to be undergoing harmonic oscillations with a frequency ω_m and power dissipation

rate $\gamma = \omega_m/Q_m$. m_{eff} is the effective mass of the mode of oscillation. The force caused by the radiation pressure is

$$F_{RP}(t) = \frac{\zeta}{c}\frac{|a|^2}{t_{rt}} \tag{2.4}$$

where ζ is a nondimensional parameter which equals $2\pi n$ for the whispering gallery mode with a refractive index of n. t_{rt} is the cavity round trip time and F_L denotes the random Langevin force F_L and obeys

$$\langle F_L(t)F_L(t')\rangle = \gamma k_B T m_{\text{eff}}\delta(t-t'). \tag{2.5}$$

$\langle\rangle$ is the ensemble average, k_B is the Boltzmann constant, T is the temperature, and δ is the Dirac delta function. The Langevin force ensures that the Fluctuation-Dissipation Theorem is satisfied. The total steady state energy without laser pumping is given by

$$E_{\text{tot}} = \int_0^\infty \omega^2 m_{\text{eff}}|\chi(\omega)F_L(\omega)|^2 d\omega = k_B T. \tag{2.6}$$

χ is the mechanical susceptibility and is given by

$$\chi(\omega) = \frac{1}{m_{\text{eff}}(i\omega\Gamma + \omega_m^2 - \omega^2)}. \tag{2.7}$$

It is particularly interesting to note that mechanical amplification is provided when the laser pump is blue-detuned ($\Delta > 0$) from the cavity mode and mechanical damping, cooling, is provided when the the laser pump is red-detuned ($\Delta < 0$) from the optical mode [19]. Typical values of the fundamental mechanical breathing mode of a microdisk are given in Table 2.1.

f_0 [MHz]	Q	m_{eff} [ng]
57.8	2,900	15

Table 2.1: Typical values of the fundamental mechanical breathing mode of a microdisk in air [34].

Equations (2.1) and (2.2) pertain to optomechanical systems where the optical cavity acts as the mechanical resonator. In cavity optomechanical sensors for AFM, such as the one shown in Figure 1.2, a parameter $g = d\omega/dY$ describes the rate of change of the optical cavity frequency as a change in the displacement of the nanobeam. A typical value for $g = 0.5\,\text{GHz/nm}$ [34].

2.2 Statistical Mechanics

Statistical mechanics is used to connect the stochastic fluctuations of the nanobeam's tip with the dissipation in the system. This connection allows the stochastic fluctuations to be

from deterministic numerical simulations. The stochastic fluctuations of the nanobeam's tip are important because they can be used to determine the stiffness of the nanobeam [31]. Furthermore, the thermal noise of an experimental system sets the measurement's ultimate force sensitivity. Next, the properties of the autocorrelation and the noise spectrum G and presented.

2.2.1 Autocorrelation

The autocorrelation function measures the correlation between the tip displacement at one time with tip displacement at another time [22]. The autocorrelation function is the time series analog to the correlation coefficient of a single statistic. The autocorrelation function of a stochastic process can be defined as

$$\langle y(0)y(\tau)\rangle = \lim_{\epsilon\to\infty} \frac{1}{\epsilon} \int_{-\epsilon/2}^{\epsilon/2} y(t)y(t+\tau)dt \tag{2.8}$$

where y is the stochastic fluctuations of the tip displacement from equilibrium. The autocorrelation function has the following properties [22]:

1. The autocorrelation function is an even function of t; and
2. $\langle y(0)y(0)\rangle \geq |\langle y(0)y(t)\rangle|$.

2.2.2 Noise Spectrum

The noise spectrum G provides a measure of tip displacement as a function of frequency due to the Brownian force. The noise spectrum can be determined from the autocorrelation of the equilibrium fluctuations [24]

$$G(\omega) = 4\int_0^\infty \langle y(0)y(t)\rangle \cos(\omega t)dt. \tag{2.9}$$

The noise spectrum G has the following properties [22]:

1. G is an even function of the angular frequency ω;
2. G is a real function; and
3. G is non-negative.

2.2.3 Fluctuation-Dissipation Theorem and Linear Response

The Fluctuation-Dissipation Theorem relates the dissipation in a system to the system's fluctuations from equilibrium. Einstein hypothesized this relationship because he realized that the same molecular processes cause both the fluctuations and the dissipation [10]. An example of a molecular process that causes fluctuations and dissipation is thermal bombardment of fluid particles on a cantilever. The Fluctuation-Dissipation Theorem is applied to the tip of the cantilever as it relaxes back to equilibrium from a step force. If the step force is applied in the distant past and then removed at $t = 0$ the Fluctuation-Dissipation Theorem yields [10, 25]

$$\langle y(0)y(t)\rangle = k_B T \frac{Y(t)}{F_0}, \tag{2.10}$$

where $y(t) = Y(t) - \langle Y\rangle$ is the fluctuations in $Y(t)$ from the time-independent equilibrium average $\langle Y\rangle$, $\langle y(0)y(t)\rangle$ is the autocorrelation of the fluctuations in the tip displacement, and F_0 is the magnitude of the step force. For Eq. (2.10) to be valid the magnitude of step force F_0 must be small enough that the system's response is linear. It is worth noting that Eq. (2.10) is not limited by any geometric constraints and is independent of the sources of dissipation. Some possible sources of dissipation are fluid damping, support loss and thermoelastic loss.

2.3 Modeling Optomechanical Sensors for AFM

Cavity optomechanical sensors for atomic force microscopy consist of a nanobeam wrapped around a microdisk optical resonator. In typical applications for atomic force microscopy the sample and the optomechanical sensor are immersed in a viscous fluid such as water. The fluid is the dominant dissipative mechanism so the fluid-solid interaction must be studied to determine the stochastic behavior of the system [30]. Other sources of dissipation include support loss and thermoelastic loss [21]. The fluid and the nanobeam are modeled as continuous media. This assumption is valid for gases if the Knudsen number $\mathrm{Kn} = \lambda/w \lesssim 0.3$ where λ is the mean free path [30, 33].

2.3.1 Modeling the nanobeam

A Lagrangian reference frame is used for the to model the nanobeam where the field variables are a function of initial position and time. For example the displacement field $\vec{Y} = \vec{Y}(\vec{Y_0}, t)$ where $\vec{Y_0}$ is the initial position and t is the time. The body forces applied to the solid are negligible so the time rate of change of the linear momentum per unit volume of the solid is

given by the local resultant of the surface forces per unit volume

$$\rho_s \frac{d^2\vec{Y}}{dt^2} = \nabla \cdot \boldsymbol{\sigma}_s \tag{2.11}$$

where ρ_s is the density and $\boldsymbol{\sigma}_s$ is the stress tensor. There are no body couples applied so the stress tensor, $\boldsymbol{\sigma}_s$ is symmetric by the balance of angular momentum. Hooke's constitutive relation is used to relate the stress and strain

$$\boldsymbol{\sigma}_s = \lambda_s \operatorname{tr} \boldsymbol{e}_s \boldsymbol{I} + 2\mu_s \boldsymbol{e}_s, \tag{2.12}$$

where $\lambda_s = \frac{\nu E}{(1+\nu)(1-2\nu)}$ and $\mu_s = \frac{E}{2(1+\nu)}$ are the Lamé constants, $\boldsymbol{I}$ is the 3 by 3 identity matrix and

$$\boldsymbol{e}_s = \frac{1}{2}\left(\nabla\vec{Y} + \left(\nabla\vec{Y}\right)^\top\right) \tag{2.13}$$

is the stretching tensor and $()^\top$ denotes a transpose.

2.3.2 Modeling the Fluid

Since the solid boundaries are moving an Arbitrary-Lagrangian-Eulerian (ALE) coordinate system is used for the fluid domain. The ALE coordinate system accounts for the displacement of the computational domain. A dependent variable in an ALE coordinate system is a function of position in the computational domain and time,

$$f(\vec{x}, t) = f(\vec{\zeta} + \vec{d}(\vec{\zeta}, t), t) \tag{2.14}$$

where the components of $\vec{\zeta}$ are the local coordinates and $\vec{d}(\vec{\zeta}, t)$ accounts for the displacement of the moving local coordinates. The total time derivative of $f(\vec{x}, t)$ in the ALE coordinate system is given by

$$\frac{Df(\vec{x}, t)}{Dt} = \frac{\partial f}{\partial t} + \frac{\partial \vec{x}}{\partial t} \cdot \frac{\partial f}{\partial \vec{x}} = \frac{\partial f}{\partial t} + \vec{V}_p \cdot \frac{\partial f}{\partial \vec{x}} \tag{2.15}$$

where

$$\vec{V}_p = \frac{\partial \vec{x}}{\partial t} = \frac{\partial \vec{d}}{\partial t} \tag{2.16}$$

is the "probe velocity" and accounts for the movement of the local coordinates. If $\vec{V}_p$ is set to the fluid velocity Eq. (2.15) represents the co-moving derivative in the Eulerian coordinate system and if $\vec{V}_p$ is set to zero Eq. (2.15) represents the time derivative in the Lagrangian coordinate system. The balance of mass gives the continuity equation

$$\frac{\partial \rho_f}{\partial t} + \nabla \cdot (\rho_f \vec{v}) = 0 \tag{2.17}$$

where $\vec{v}$ is the fluid velocity and the fluid density ρ_f is assumed to be slightly compressible. The density is given by

$$\rho_f = \rho_0 \left(1 + \frac{P}{\kappa}\right) \tag{2.18}$$

where P is the local pressure, ρ_0 is the nominal density and κ is the fluid bulk modulus. The fluid is assumed to be slightly compressible because the fluid domain is bounded by a rigid container. Assuming incompressible flow would make the continuity equation difficult to satisfy. The fluid is modeled as a slightly compressible, Newtonian fluid with negligible body forces so the time rate of change of linear momentum per unit volume of the fluid is given by the local resultant of the surface forces per unit volume

$$\rho_f \frac{D\vec{v}}{Dt} = \nabla \cdot \boldsymbol{\sigma}_f. \tag{2.19}$$

There are no body couples applied so the stress tensor is symmetric by the balance of angular momentum. The fluid is assumed to be Newtonian so the constitutive relation relating the stress and strains is given by

$$\boldsymbol{\sigma}_f = (-P + \lambda_f \operatorname{tr} \boldsymbol{e}_f)\boldsymbol{I} + 2\mu_f \boldsymbol{e}_f, \tag{2.20}$$

where Stokes's hypothesis gives $\lambda_f = -\frac{2}{3}\mu_f$, $\operatorname{tr} \boldsymbol{e}_f$ is the trace of the rate of strain tensor, and μ_f is the viscosity. The rate of strain tensor is

$$\boldsymbol{e}_f = \frac{1}{2}\left(\nabla\vec{v} + (\nabla\vec{v})^\top\right). \tag{2.21}$$

It can be more straight forward to numerically model the fluid as slightly compressible, but it is valid to model the fluid as incompressible. Modeling the fluid as incompressible yields the non-dimensional Navier-Stokes equations

$$\mathrm{R}\frac{\partial\vec{v}}{\partial t} + \mathrm{Re}(\vec{v}\cdot\nabla)\vec{v} = -\nabla P + \nabla^2\vec{v}, \tag{2.22}$$

$$\nabla \cdot \vec{v} = 0 \tag{2.23}$$

where R is the frequency based Reynolds number, also called the Stokes number, and Re is the velocity based the Reynolds number. The frequency based Reynolds number is

$$\mathrm{R} = \frac{L^{*2}}{\nu_f T^*} \tag{2.24}$$

where $L^* = w/2$ is the characteristic length and $T^* = 2\pi/\omega$ is the characteristic timescale where ω is radial frequency. The frequency based Reynolds number expresses the ratio of local inertia and viscous forces. The velocity based Reynolds number is

$$\mathrm{Re} = \frac{U^* L^*}{\nu_f} \tag{2.25}$$

where U^* is the characteristic velocity and $L^* = w/2$ is the characteristic length scale. The Reynolds number expresses the ratio between convective inertia and viscous forces. The nanobeam's frequency of oscillation is typically in the megahertz, while the amplitude is typically a few nanometers. In this case $\mathrm{Re} \ll 1$, so the convective inertia term is negligible and the governing equations become linear. However, the frequency based Reynolds number is $\mathrm{R} \approx 1$, so the local inertia can not be neglected.

2.3.3 Boundary Conditions

The fluid and the nanobeam are coupled through kinematic and dynamic boundary conditions. The kinematic boundary condition on the fluid-solid interface is

$$\vec{d_f} = \vec{d_s} \tag{2.26}$$

where $\vec{d_f}$ and $\vec{d_s}$ are the fluid and nanobeam displacements at the interface. The dynamic boundary condition is

$$\vec{n} \cdot \boldsymbol{\sigma}_f = \vec{n} \cdot \boldsymbol{\sigma}_s \tag{2.27}$$

where $\vec{n}$ is the outward pointing normal.

Chapter 3

Numeric Modeling

3.1 Introduction

ADINA® is a commercial finite element analysis software. The ADINA® fluid-solid interaction capability is used to perform the deterministic numerical calculations. The fluid and solid models are coupled together through direct coupling. In direct coupling the fluid model and solid model equations are combined and treated as one system. One stiffness matrix is created, linearized and solved using an iterative algorithm. The direct coupling algorithm is well suited for "soft" structures in fluid flows when iterative coupling has difficulty [3]. A composite method integration scheme is used to obtain solutions at $t + \Delta t$ by using two consecutive sub-time-steps. The composite method is second order accurate and is unconditionally L-stable [3].

A finite element model is used to model the response of the nanobeam in a viscous fluid. The goal is to include the dominant features of cavity optomechanical systems for AFM, while maintaining an acceptable computation time. The dominant features that dictate the stochastic response of the mechanical degrees of freedom are the nanobeam, the fluid in which the device is immersed and the wall effects caused the close proximity of the microdisk to the nanobeam. The optomechanical interaction is not included in the model. The nanobeam is modeled as an isotropic elastic three dimensional solid and the microdisk is modeled as a rigid body. The sharp tip of the nanobeam is blunted to increase element quality. This is not a major assumption as the Reynolds number of the flow is very small. The support structure for the nanobeam and the microdisk are not modeled and instead the displacement is fixed where the nanobeam meets the support structure. The fluid is assumed to be slightly compressible. Both air and water are used as fluids in the simulations as these fluids are commonly encountered in practice. Solid walls bound the fluid that immerses the optomechanical model. The solid walls are far enough away from the nanobeam so they have a negligible affect on the dynamics of the nanobeam.

The computational domain consists of the solid model and the fluid model as seen in Figure 3.1. Two planes of symmetry are used to reduce the computational effort as seen in Figure 3.2.

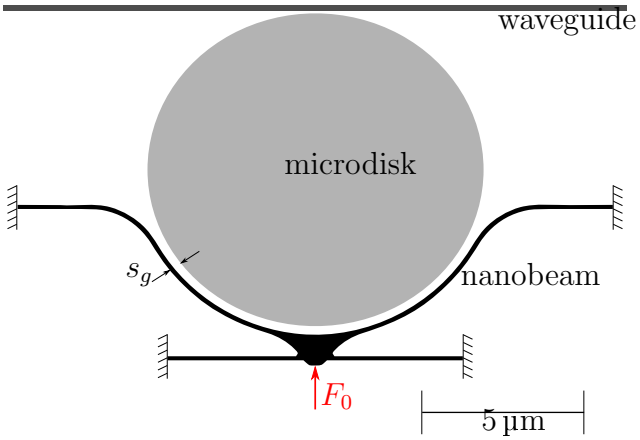

Figure 3.1: A schematic of a cavity optomechanical system that consists of a fiber taper wave guide that is coupled to a 10 µm diameter microdisk optical resonator. A force F_0 is applied to the tip of the nanobeam that wraps around the microdisk optical resonator. The gap between the nanobeam and the optical microdisk resonator is $s_g = 100\,\text{nm}$. The nanobeam is anchored on four faces.

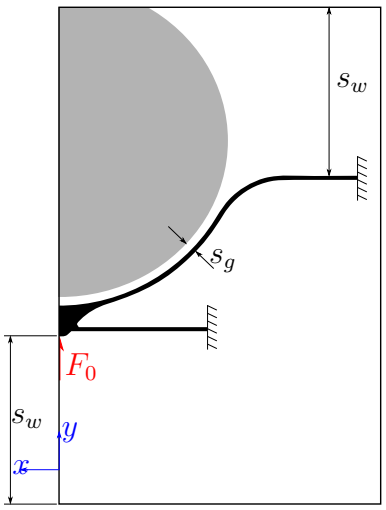

Figure 3.2: The computational domain used to model the optometrical sensor. The microdisk is modeled as a fixed rigid body, the nanobeam is modeled as an isotropic elastic solid, and the fluid is modeled as a slightly compressible Newtonian fluid. The blue box denotes the solid walls that bound the fluid.

3.2 Constructing the Solid Model

The solid model represents a nanobeam used in recent experiments on cavity optomechanical sensors for AFM [34]. The nanobeam wraps around a 10 µm diameter microdisk optical resonator with a 100 nm gap between the nanobeam and the microdisk optical resonator. The nanobeam has a height of $h = 100$ nm and and a width of $w = 260$ nm. The nanobeam is meshed with eight node linear block elements as illustrated in Figure 3.3.

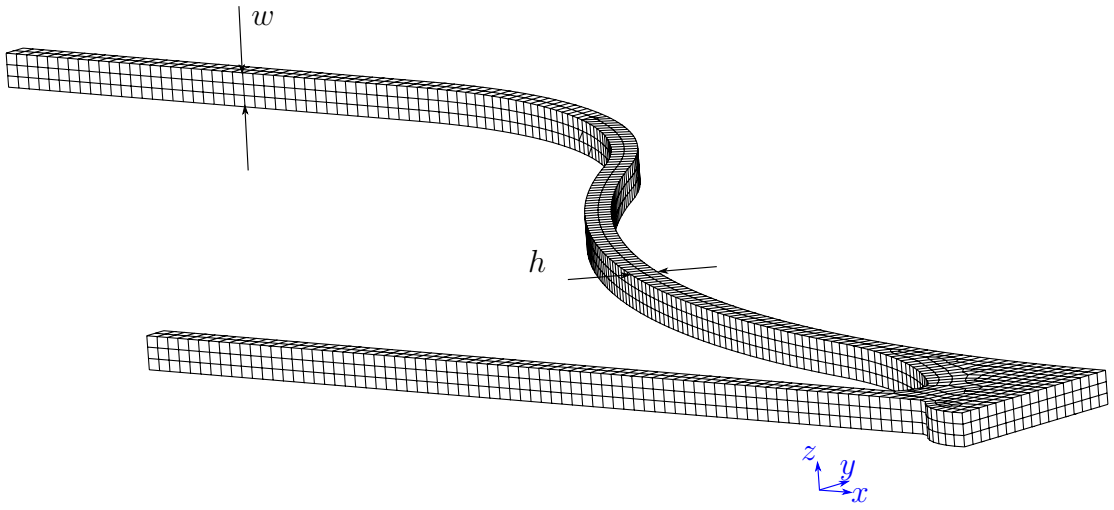

Figure 3.3: The finite element mesh of the nanobeam. The x-y plane and the y-z plane are used as planes of symmetry. The nanobeam has a width of $w = 260$ nm and a height of $h = 100$ nm. The nanobeam is meshed with eight node linear block elements.

The tip of the nanobeam would interact with a sample in tapping mode operation and move the nanobeam in plane with the microdisk optical resonator. A step force is applied to the tip of nanobeam. The tip of the nanobeam is blunted to increase the quality of the elements near the tip. This is not a major assumption due to the small Reynolds number of the flow. The nanobeam is anchored on four faces to represent the beams attachments to the supports on the microchip. Two planes of symmetry are used in order to reduce the computation time of the simulations. The following criteria need to be symmetric to utilize a plane of symmetry [29]:

1. physical properties;
2. geometry; and
3. sources and sinks.

The x-y plane and y-z plane in Figure 3.1 are planes of symmetry that are used to reduce the computational effort and time. The nanobeam is created in Autodesk Inventor® and imported into ADINA® as a Parasolid 9 model. Fluid-solid interfaces are specified on all the faces of the solid model. All degrees of freedom are fixed on the anchored faces. Also, the normal displacement is set to zero on the planes of symmetry. The dimensions of the nanobeam are provided in Figure 3.4. The beam is assumed to be isotropic and the material properties are provided in Table 3.1.

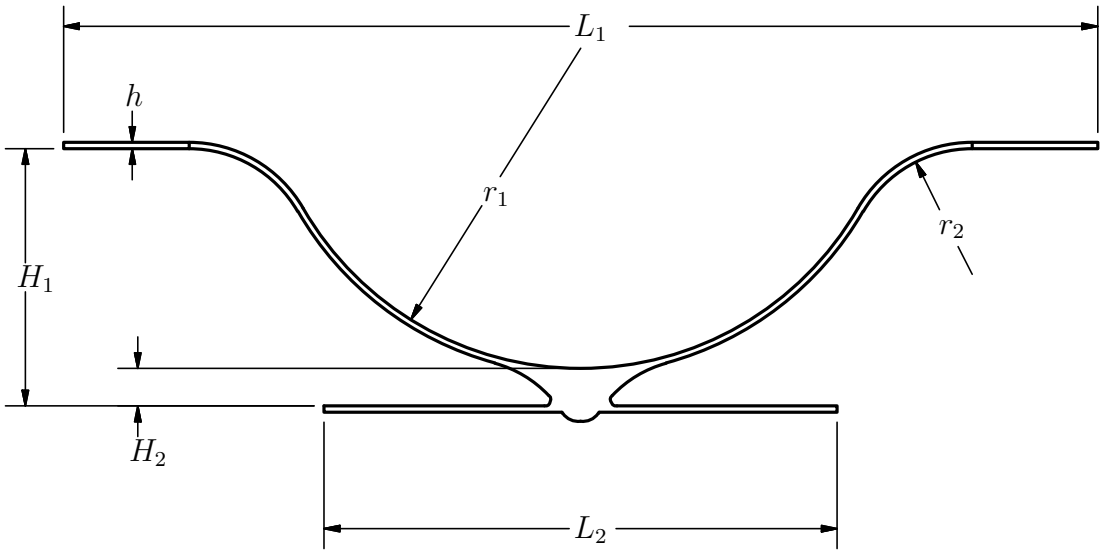

Figure 3.4: Dimensions of the x-y projection of the nanobeam. L_1 is the distance between the faces that anchor the back supports, L_2 is the distance between the faces that anchor the front supports, H_1 is the distance between the back supports and the front supports, H_2 is the distance between the front supports and the apex of the curve defined by r_1, the portion of the nanobeam that wraps around the microdisk is defined by r_1, and r_2 is the radius of curvature that creates a smooth transition to the back supports. The values of the dimensions illustrated in this figure are provided in Table 3.1.

E	ρ_s	L_1	L_2	H_1	H_2	r_1	r_2	h	w
[GPa]	[kg/m^3]	[μm]	[μm]	[μm]	[μm]	[μm]	[μm]	[μm]	[μm]
174	2320	16.57	8.17	4.1	0.6	5.1	2	0.1	0.26

Table 3.1: The dimensions and material properties of the nanobeam. The dimensions are illustrated in Figure 3.4.

3.3 Constructing the Fluid Model

The nanobeam is completely immersed in fluid. A box is created in ADINA-M® and the solid model is subtracted from the box using a Boolean operation. The same x-y plane and y-z plane that are used in the solid model are used in the fluid model as planes of symmetry. Fluid-solid interfaces are specified on all the faces coincident with the solid model. A wall with a slip condition is applied to the planes of symmetry. Walls without a slip condition are applied on the remaining faces that bounded the fluid. The faces coincident with the solid model are subdivided to match the subdivisions of the solid model. The rest of the faces are subdivided with a larger uniform length. The edges on the y axis are subdivided with a bias so that the element quality is high near the tip of the beam. The fluid model is enclosed in a rigid container, which is why the fluid is modeled as slightly compressible. Modeling the fluid as slightly compressible allows the continuity equation to be satisfied more easily. Four node linear tetrahedral elements are used to mesh the fluid domain. The ADINA® Dulaney meshing algorithm creates the unstructured mesh of the fluid domain in Figure 3.5.

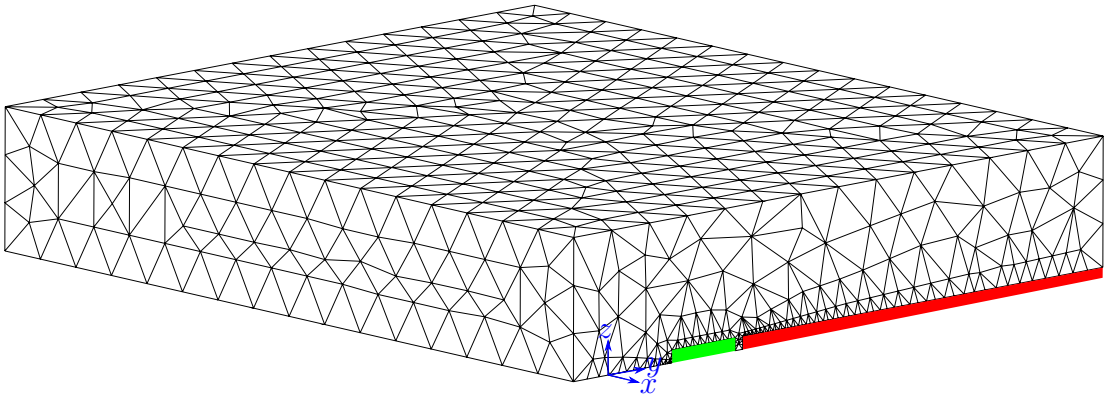

Figure 3.5: An isometric view of the fluid mesh. The fluid domain is meshed with four node linear tetrahedral elements. The unstructured mesh is created using a Dulaney meshing algorithm. The x-y plane and y-z plane of symmetry are used to reduce the computational effort. The intersection of the nanobeam and the y-z plane is shown in green. The intersection of the microdisk and the y-z plane is shown in red.

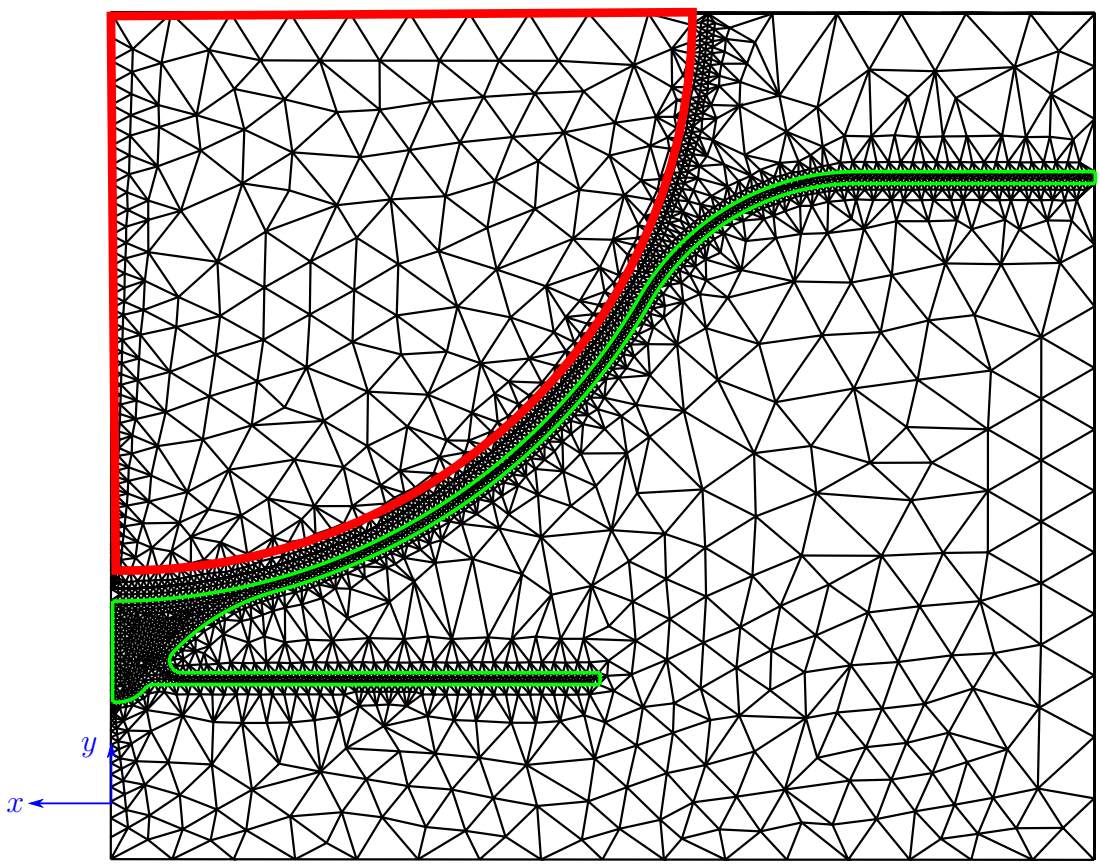

Figure 3.6: A view of the x-y plane of the fluid mesh. The nanobeam is outlined in green and the microdisk is outlined in red. The edge y axis are subdivided with a biased to maintain the a high element quality near the tip of the beam.

3.4 Domain Independence

The fluid domain is bounded by solid walls. These solid walls modify the fluid flow and increase the damping of the nanobeam. The separation between the solid walls and the nanobeam are varied to confirm that the solid walls bounding the fluid domain do not have a significant effect on the fluid flow or the damping. The separation between the walls and the nanobeam are shown in Figure 3.2. The separation denoted in Figure 3.2 also extends in the out-of-page direction. The effect of the separation between the solid walls and the nanobeam on the flow and the damping can be understood by considering the Stokes length

$$\delta_s = \sqrt{\frac{\nu_f}{\omega}}, \tag{3.1}$$

where ν_f is the kinematic viscosity, and ω is radial frequency of nanobeam [32]. The Stokes length gives a scaling for the size of the unsteady viscous boundary layer. The natural frequency yields

$$\delta_0 = \sqrt{\frac{\nu_f}{\omega_0}} \cong 132\,\text{nm}. \tag{3.2}$$

Contour plots, such as the one shown in Figure 3.7, of the magnitude of fluid velocity are used to illustrate how the flow field is altered by the solid walls that bound the fluid domain.

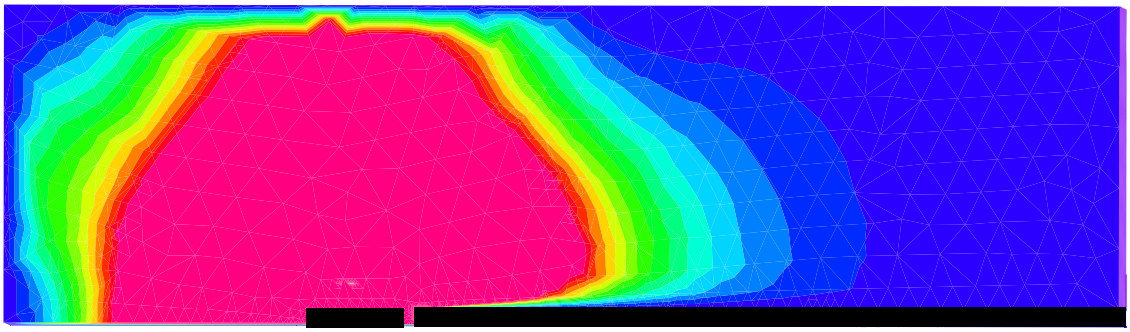

Figure 3.7: Fluid velocity magnitude contour plot on the y-z plane. The fluid velocity magnitude is 3.5 mm/s (red), 2.75 mm/s (yellow) and 2 mm/s (green). The wall separation is $s_w = 20\delta_0$. The black rectangles show where the nanobeam and the microdisk intersect the y-z plane.

Figure 3.8 illustrates that the solid walls have a negligible effect on the damping of the cantilever when the walls are separated from the nanobeam by $s_w = 10\delta_0$.

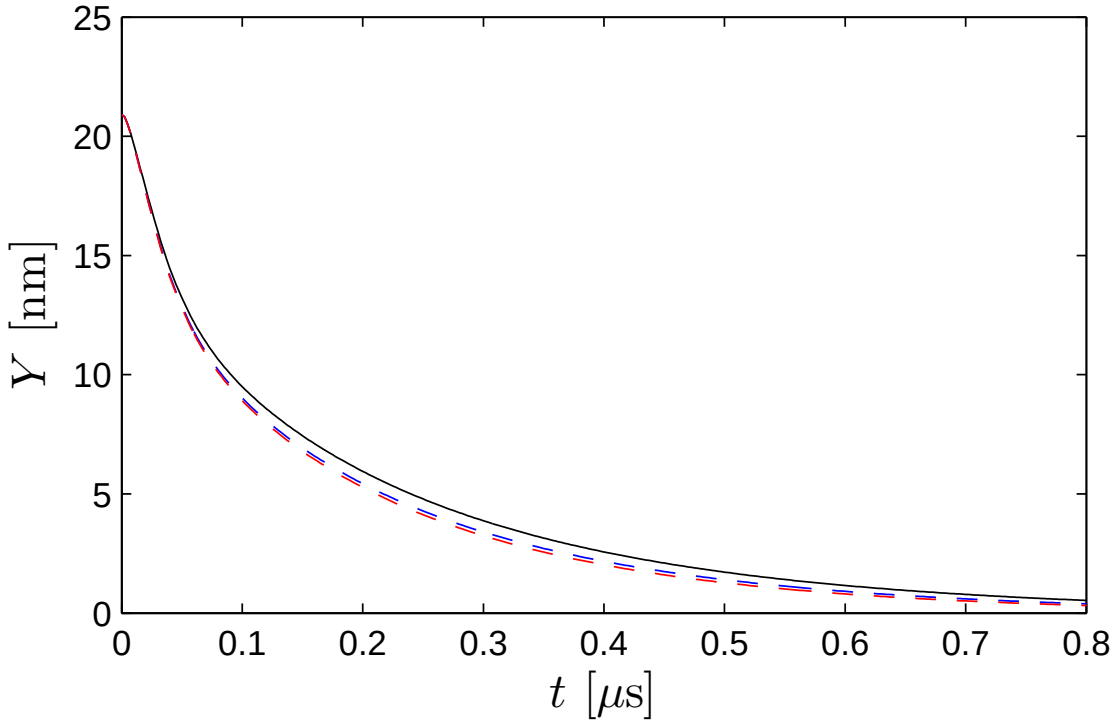

Figure 3.8: The nanobeam's tip displacement released from a step force at $t = 0$. The microdisk is modeled as a rigid body. The wall separation is $s_w = 5\delta_0$ (solid black line), $s_w = 10\delta_0$ (dashed blue line), and $s_w = 20\delta_0$ (dashed red line).

The gap $s_g = 0.75\delta_0$ between the nanobeam and the microdisk has a significant effect on the damping of the nanobeam. A wall vicinity of $s_w = 10\delta_0 = 1.32\,\mu\text{m}$ is sufficient to ensure the wall effects on the nanobeam are negligible. However, if the microdisk is omitted a wall separation of $s_w = 20\delta_0$ is needed to ensure the wall effects are negligible.

3.4.1 Influence of the microdisk

The microdisk is omitted and the nanobeam is released from a step force at $t = 0$. The microdisk significantly increases the viscous damping of the nanobeam. This is observed by comparing Figure 3.8 and Figure 3.9. Figure 3.9 illustrates that a wall separation of $s_w = 20\delta_0$ or greater is needed to ensure the wall effects are negligible.

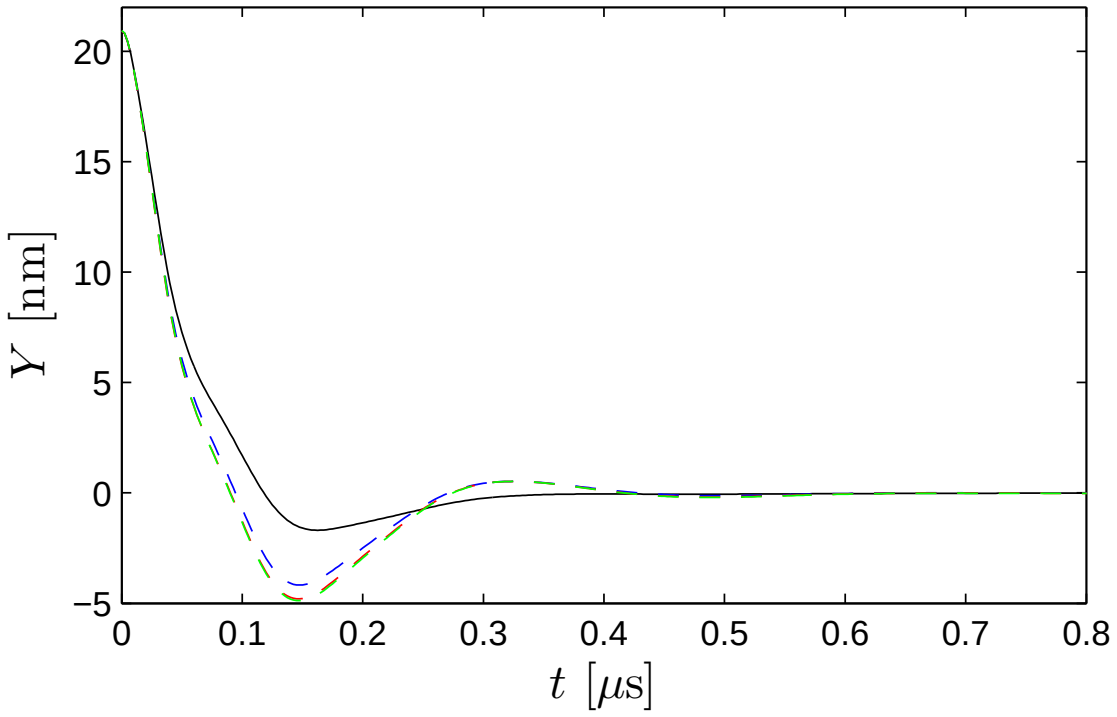

Figure 3.9: The nanobeam's tip displacement released from a step force at $t = 0$ in water. The microdisk is omitted from the simulation. A wall separation of $s_w = 5\delta_0$ (solid black line), $s_w = 10\delta_0$ (dashed blue line), $s_w = 20\delta_0$ (dashed red line), and $s_w = 40\delta_0$ (dashed green line).

The effect of s_g on the nanobeam dynamics is illustrated in Figure 3.10.

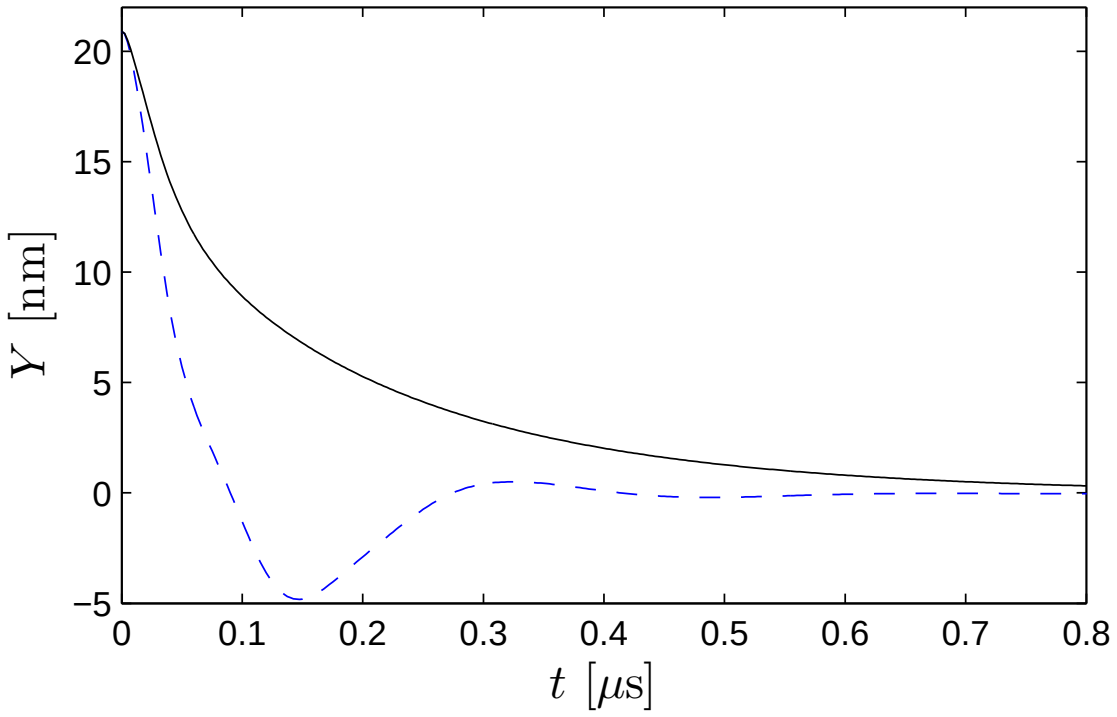

Figure 3.10: The nanobeam's tip displacement released from a step force at $t = 0$ in water. The dynamics of the nanobeam with microdisk included (solid black line) and with the microdisk omitted (dashed blue line) are compared. The wall separation is $s_w = 20\delta_0$.

The resonator is not overdamped when the microdisk is omitted. A larger separation is needed when the microdisk is omitted to ensure the wall effects are negligible.

3.5 Mesh Independence

The generation of the finite element mesh is very important for modeling fluid-solid interactions. The mesh should represent the geometry accurately, adequately represent large gradients in the solution, and the mesh should not contain unacceptable elements. The numerical integration over the mesh elements involves transforming the elements into the master elements through a coordinate transformation. If the determinant of the Jacobian is zero then the mapping to the master elements is not one-to-one and the elements are unacceptable [29]. The mesh density is varied to ensure the mesh is adequate. The fluid mesh shown in Figure 3.5 and the solid mesh shown in Figure 3.3 are used in the mesh independence study. The mesh independence study is performed in water. The wall separation is $s_w = 10\delta_0$. The faces of the nanobeam and the microdisk are subdivided with a constant length of $\min \Delta x$. The walls that bound the fluid domain are subdivided with a

larger subdivision of length $\max \Delta x$. The edges on the y axis in Figure 3.5 are subdivided with a bias to maintain high element quality. The values of the subdivisions are given in Table 3.2.

$h/\min \Delta x$	$\delta_0/\max \Delta x$	$\max \Delta x/\min \Delta x$	N
2	5	13.2	7.2×10^4
2	2	5.28	1.1×10^5
2	1	2.64	2.7×10^5
5	1	6.6	5.65×10^5

Table 3.2: $\min \Delta x$ is the length of the subdivision on the faces of the nanobeam and the microdisk. $h = 100\,\text{nm}$ is the height of the nanobeam. $\max \Delta x$ is the number of subdivisions on the walls that bound the fluid. $\delta_0 = 132\,\text{nm}$ is the Stokes length in water. N is the total number of elements.

The subdivisions on the solid walls that bound the fluid $\max \Delta x$ are varied, while the subdivisions on the microdisk and the nanobeam $\min \Delta x$ are held fixed.

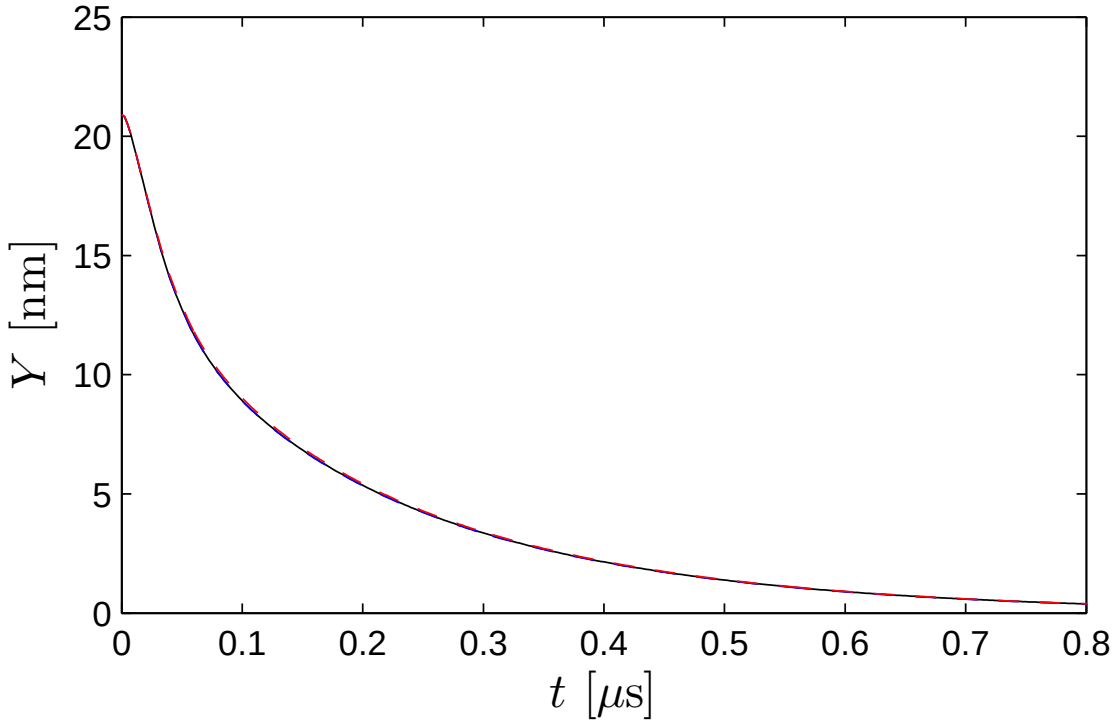

Figure 3.11: The nanobeam's tip displacement released from a step force at $t = 0$ in water. $\delta_0/\max\Delta x = 1$ (solid black line), $\delta_0/\max\Delta x = 2$ (dashed blue line) and $\delta_0/\max\Delta x = 5$ (dashed red line). The wall separation is $s_w = 10\delta_0$. The subdivisions on the microdisk and the nanobeam are held fixed; $h/\min\Delta x = 2$.

The subdivisions on the nanobeam and the microdisk $\min\Delta x$ are varied, while the subdivisions on the walls that bound the fluid $\max\Delta x$ are held fixed.

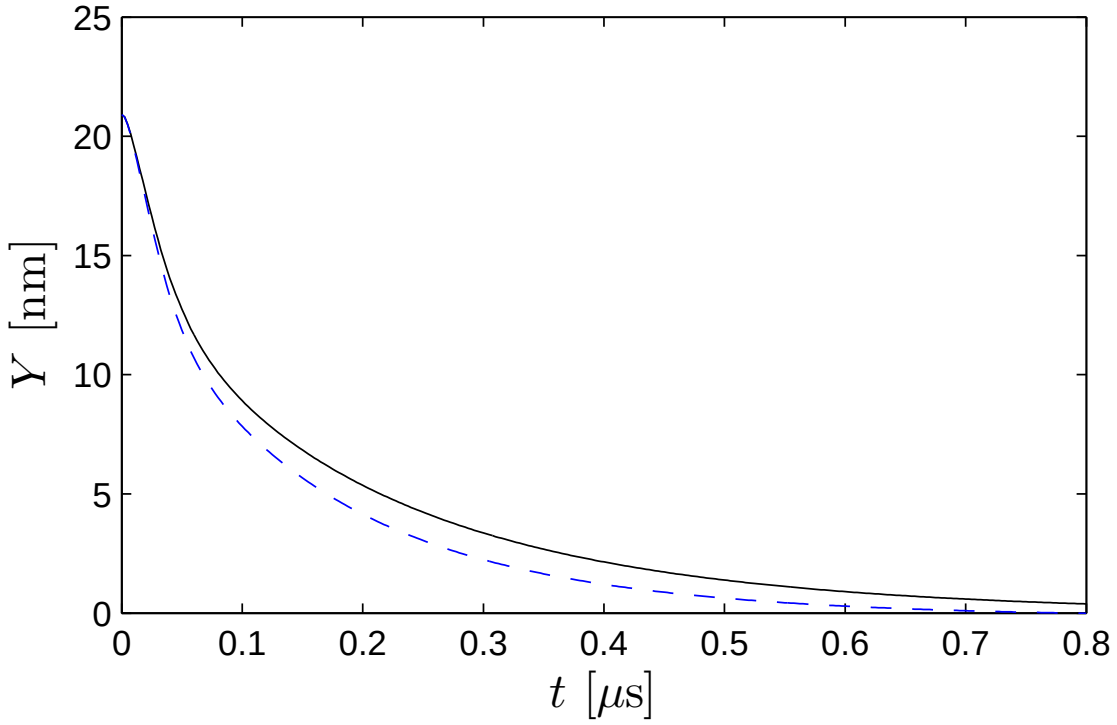

Figure 3.12: The nanobeam's tip displacement released from a step force at $t = 0$ in water. $h/\min \Delta x = 2$ (solid black line) and $h/\min \Delta x = 5$ (dashed blue line). The wall separation is $s_w = 10\delta_0$ and the subdivisions on the solid walls are $\max \Delta x = 1$. The microdisk is included.

Figure 3.12 demonstrates that as long as the number of subdivisions on the nanobeam is greater than or equal to $h/\min \Delta x = 2$ the results are not significantly impacted by number of subdivisions on the nanobeam.

3.6 Time Step Independence

The size of the time step is varied to ensure the results are independent of the time step. The fluid mesh shown in Figure 3.5 and the solid mesh shown in Figure 3.3 are used in the time step independence study. The time step study is performed in water. The wall separation, as defined in Figure 3.1 is $s_w = 10\delta_0$. $\delta_0 = 132\,\text{nm}$ is the Stokes length of the nanobeam in water based on the natural frequency in vacuum. The faces of the nanobeam and the microdisk are subdivided with a constant of length of $\min \Delta x = h/2$ where $h = 100\,\text{nm}$ is the height of the nanobeam. The walls that bound the fluid domain are subdivided with a larger subdivision of length $\max \Delta x = 5\delta_0$. The tip of the nanobeam is subjected to a step force in the distant past and released at $t = 0$. The tip velocity is greatest in the first $0.2\,\mu\text{s}$.

The time step is $\Delta t = 0.002\,\mu\text{m}$ in the first $0.2\,\mu\text{s}$ and the remaining time steps Δt are given in Table 3.3. The tip displacements are compared in Figure 3.13.

Δt [μs]	B [min/step]
0.002	1.49
0.0025	1.48
0.005	1.71
0.01	2.22

Table 3.3: Δt is the size of the time step. B is the computation time per time step. $N = 7.14 \times 10^4$ is the total number of elements. A typical simulation requires approximately 500 time steps. The wall separation is $s_w = 10\delta_0$. $\max \Delta x = 5\delta_0$ and $\min \Delta x = h/2$.

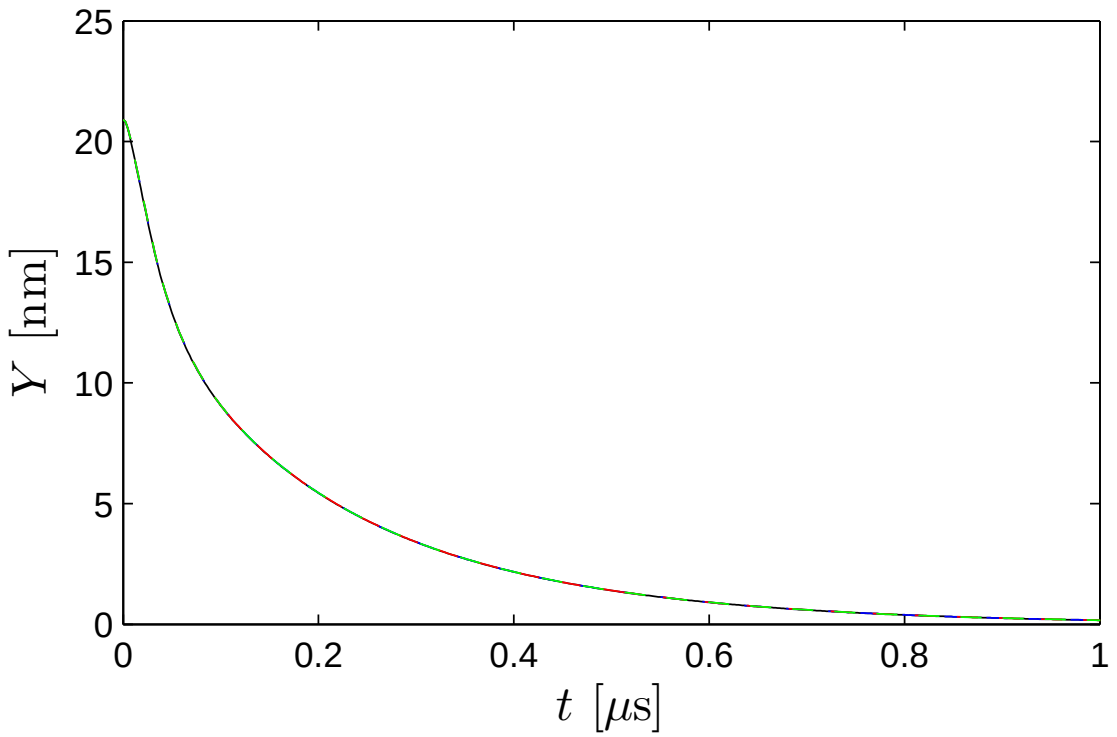

Figure 3.13: The nanobeam's tip displacement released from a step force at $t = 0$ in water. The wall separation is $s_w = 10\delta_0$. $\max \Delta x = 5\delta_0$ and $\min \Delta x = h/2$. $\Delta t = 0.002\,\mu\text{s}$ (solid black line), $\Delta t = 0.0025\,\mu\text{s}$ (dashed blue line), $\Delta t = 0.005\,\mu\text{s}$ (dashed red line), and $\Delta t = 0.01\,\mu\text{s}$ (dashed green line).

3.7 Computation Time

Because the simulations of the nanobeam in fluid can take three to six months to run, the computation time is an important factor to consider. In order to reduce the computation time from multiple months to a couple of weeks, the geometry is simplified and planes of symmetry are used. The largest reduction in computation time is achieved by using the two planes of symmetry defined by the x-y plane and the y-z plane. The planes of symmetry are shown in Figure 3.3 for the solid model and in Figure 3.5 for the fluid model. Each plane of symmetry reduces the computation time by approximately a factor of four. The criteria in Section 3.2 need to be satisfied to use a plane symmetry in a computational model [29]. The computation time is further reduced by blunting the sharp tip of the nanobeam that is illustrated in Figure 3.1. Blunting the sharp increases the element quality near the tip of the beam. Elements can overlap when the element quality is low and then the mesh would need to be reconstructed. Blunting the sharp tip is not a major assumption because the Reynolds number of the flow is very small. The computation time is directly related to the number of elements used to mesh the fluid and solid models.

The relationship between the computation time per time step B and the number elements is illustrated in Figure 3.14. The data shown in 3.14 is for the nanobeam in water. The number of elements is varied by changing the mesh density.

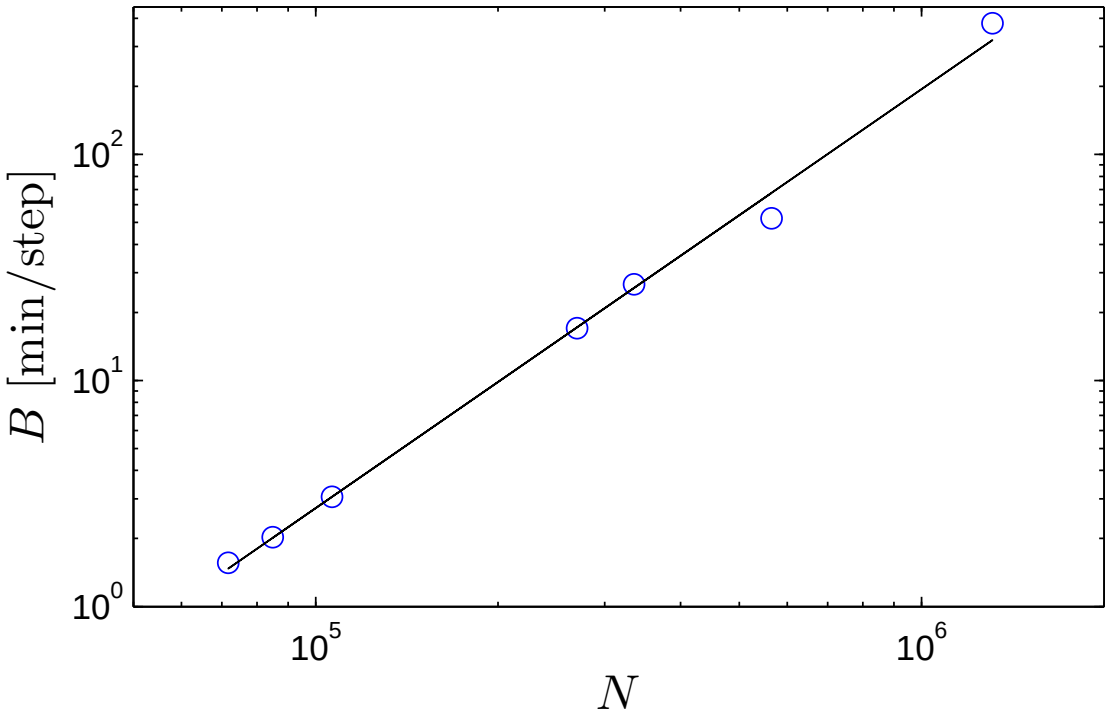

Figure 3.14: Computation time per time step B of the nanobeam in water as a function of the number of elements N (blue circles). A curve fit is fitted to the data using a least squares curve fit (solid black). The curve fit gives $B = 1.47 \times 10^{-9} N^{1.85}$.

The curve fit gives the relation $B = 1.47 \times 10^{-9} N^{1.85} \sim N^2$ where B is the computation time per time step in minutes and N is the total number of elements. The simulation for the nanobeam in water requires at least 400 time steps. Typical simulations times are provided in Table 3.4.

N	B [min/step]	total simulation time [hr]
7×10^4	1.5	13
1×10^5	3	25
3×10^5	17	142
4×10^5	23	190
6×10^5	52	300

Table 3.4: The typical computation time for different mesh resolutions of the nanobeam in water with the microdisk included. There are approximately 500 time steps for each simulation.

Chapter 4

Code Validation

The finite element code and the modeling procedure are validated by numerically calculating the noise spectrum of a Park Scientific Instruments AFM cantilever. The cantilever is a high tolerance calibration cantilever termed the C2 cantilever [12]. The C2 cantilever is chosen because of the available experimental and analytic results of [12, 25].

4.1 Validation

The C2 cantilever is 197 µm long by 29 µm wide by 2 µm and is illustrated in Figure 4.1. The C2 cantilever is modeled as a linear elastic three-dimensional solid with a Young's modulus of $E = 174\,\text{GPa}$ and a density of $\rho_s = 2320\,\text{kg/m}^3$. The C2 cantilever is immersed in water that has a viscosity of $\mu_f = 8.59 \times 10^{-4}\,\text{Pa s}$ and a density of $\rho_f = 997\,\text{kg/m}^3$. This is chosen as the test case because of the available analytical data [12, 25]. The properties of the C2 cantilever are summarized in Table 4.1.

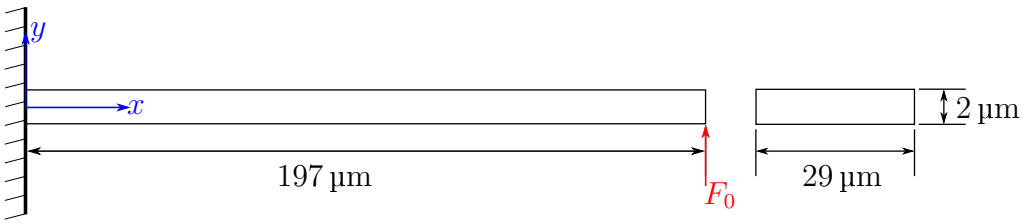

Figure 4.1: A schematic of the C2 cantilever geometry used for the validation tests. The length is 197 µm, the width is 29 µm and the height is 2 µm.

L [μm]	w [μm]	h [μm]	f_0 [kHz]	k [N/m]
197	29	2	72.1	1.32

Table 4.1: Properties of the C2 cantilever. L is the length, w is the width, h is the height, f_0 is the fundamental radial frequency in vacuum and k is the stiffness in the y direction. The Young's modulus is $E = 174\,\text{GPa}$ and the density is $\rho_s = 2320\,\text{kg/m}^3$.

4.2 Validating the Model in Vacuum

The solid model is validated in vacuum to understand if the sources of error are primarily due to the solid model alone or the modeling of the fluid-solid interaction. A step force is applied to the tip of the C2 cantilever and the tip displacement is recorded. The tip displacement is compared to the analytical solution found through modal analysis.

4.2.1 Modal Analysis

The development of Ref. [22] is followed to construct the analytic solution using modal analysis. Modal analysis uses the orthogonality of eigenfunctions and the expansion theorem. The expansion theorem states that any function representing an admissible displacement of the beam can be expanded in the absolutely and uniformly convergent series of the eigenfunctions [22].

Governing Equations and Boundary Conditions

The governing equation is determined from Euler-Bernoulli Beam Theory. The following assumptions need to be valid [22]:

- The length of the beam is much greater than the height of the beam, $L \gg h$;
- The rotational inertia and the shear deformation can be ignored; and
- The beam does not become too wrinkled, $L \gg$ radius of curvature.

The governing equation of motion for the beam is

$$EI\frac{\partial^4 Y(x,t)}{\partial x^4} + f(x,t) = m\frac{\partial^2 Y(x,t)}{\partial t^2} \tag{4.1}$$

where x ranges from zero to one because it is nondimensional, E is the Young's modulus, I is the second moment of area, m is the mass per unit length, $Y(x,t)$ is the displacement of the beam, and $f(x,t)$ is the force per unit length. The displacement at the wall is

$$Y(0,t) = 0 \tag{4.2}$$

and the slope of the displacement at the wall is

$$\left.\frac{\partial Y(x,t)}{\partial x}\right|_{x=0} = 0. \tag{4.3}$$

The moment at the tip is zero

$$EI\left.\frac{\partial^2 Y(x,t)}{\partial x^2}\right|_{x=1} = 0 \tag{4.4}$$

and the shear force at the tip of the beam is equal to the applied force

$$-EI\left.\frac{\partial^3 Y(x,t)}{\partial x^3}\right|_{x=1} = F. \tag{4.5}$$

The initial displacement is

$$Y(x,0) = 0 \tag{4.6}$$

and the initial velocity is

$$\frac{\partial Y(x,0)}{\partial t} = 0. \tag{4.7}$$

The boundary conditions need to be homogenous to utilize modal analysis. The only non-homogeneous boundary condition is Eq. (4.5), which is transformed into a homogenous boundary condition by representing the applied force as a distributed force over a small area near the tip. As a result Eq. (4.1) becomes

$$EI\frac{\partial^4 Y(x,t)}{\partial x^4} + F\delta(x-1) = m\frac{\partial^2 Y(x,t)}{\partial t^2} \tag{4.8}$$

and boundary condition Eq. (4.5) becomes

$$-EI\left.\frac{\partial^3 Y(x,t)}{\partial x^3}\right|_{x=1} = 0. \tag{4.9}$$

The Eigenvalue Problem

The characteristic equation of the eigenvalue problem associated with Eq. (4.8) is

$$\cos(\alpha)\cosh(\alpha) + 1 = 0, \tag{4.10}$$

where $\alpha^4 = \omega^2 m/EI$. The first six roots of the characteristic Eq. (4.10) are determined by a combination of graphical and numerical root finding methods. $\phi_1 = \cos(\alpha)$ and $\phi_2 =$

$-1/\cosh(\alpha)$ are plotted against one another in Figure 4.2 and their intersections are used as initial guesses for the roots of Eq. (4.10).

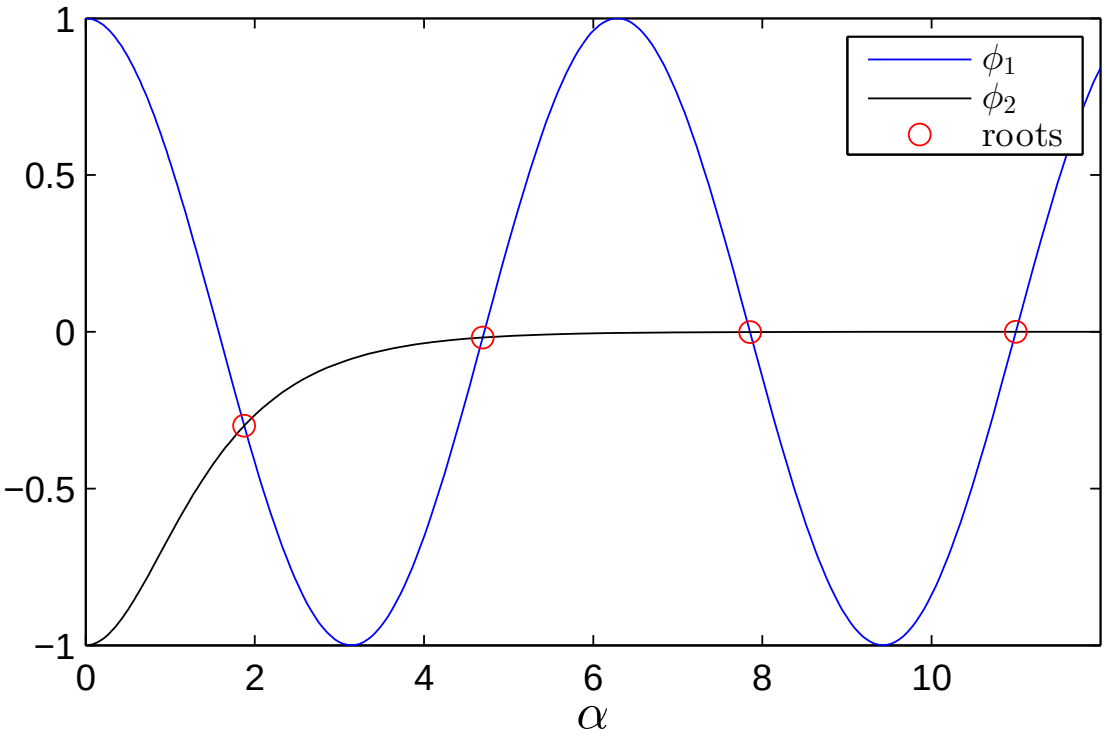

Figure 4.2: Graphical root finding method to solve the transcendental eigenvalue equation. The roots occur at the intersections of ϕ_1 and ϕ_2.

After the first four roots, the roots are located at approximately the crossing of ϕ_1 with the horizontal axis so that $\alpha \cong \frac{\pi}{2}(2n-1)$ for $n > 4$; This behavior is confirmed by examining Figure 4.2 and the limiting behavior of ϕ_2. The natural frequencies are found from the roots of Eq. (4.10) and by noting that the natural frequencies are given by $\omega_r = \alpha^2\sqrt{EI/mL^4}$. The first five natural frequencies of the C2 cantilever are listed in Table 4.2.

ω_0 [rad/s]	ω_1 [rad/s]	ω_2 [rad/s]	ω_3 [rad/s]	ω_4 [rad/s]
4.53×10^5	2.84×10^6	7.95×10^6	1.56×10^7	2.57×10^7

Table 4.2: The first five natural frequencies of the C2 cantilever determined from modal analysis.

The eigenfunctions corresponding to Eq. (4.8) and the boundary conditions Eq. (4.2)-(4.4)

and (4.9) are

$$Y_r(x) = A_r(\sin(\alpha_r x) - \sinh(\alpha_r x) - \frac{\sin(\alpha_r) + \sinh(\alpha_r)}{\cos(\alpha_r) + \cosh(\alpha_r)} (\cos(\alpha_r x) - \cosh(\alpha_r x)) . \tag{4.11}$$

The natural modes are plotted to confirm that they represented admissible displacements. The first four natural modes are plotted in Figure 4.3.

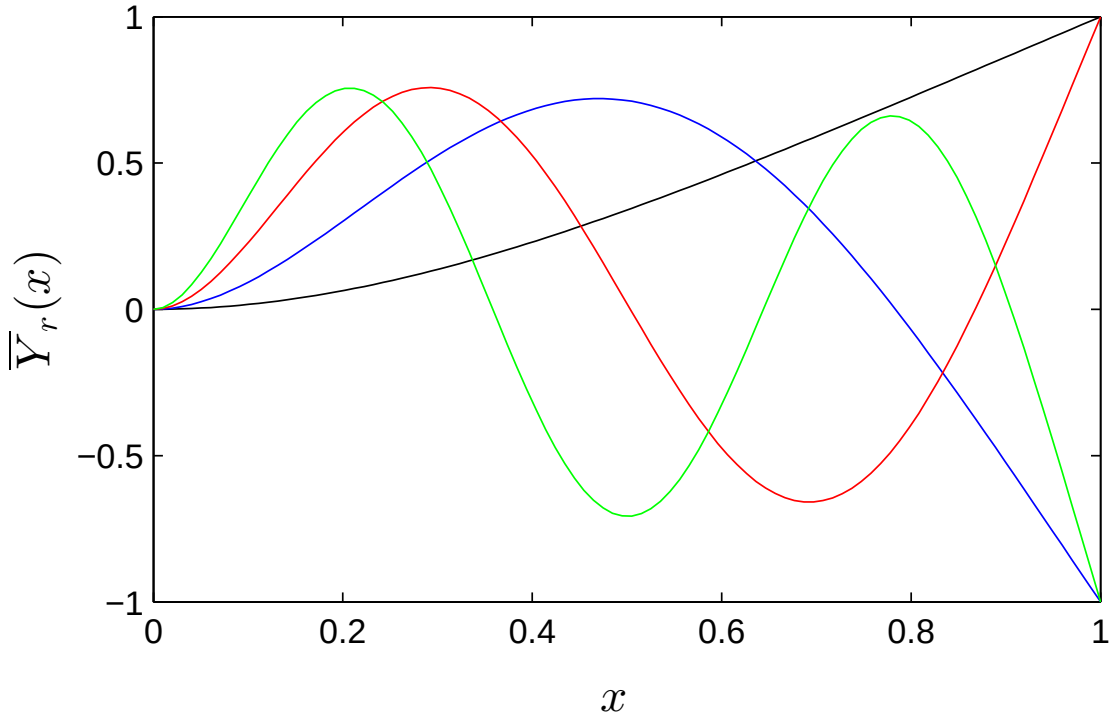

Figure 4.3: The first four natural modes of a cantilever. The modes are normalized so their maximum amplitudes are unity.

The natural modes represent admissible displacements by examining the displacements and slopes of the natural modes at the boundaries in Figure 4.3.

Orthonormalization

The natural modes are normalized so they are orthonormal with respect to the mass per unit length m using the MATLAB® quad function so that

$$m \int_0^1 Y_r(x) Y_s(x) dx = \delta_{rs} \tag{4.12}$$

where δ_{rs} is the Kronecker delta function. As a result

$$EI \int_0^1 Y_s(x) \frac{d^4 Y_r(x)}{x^4} dx = w_r^2 \delta_{rs}. \tag{4.13}$$

Equation (4.12) and Eq. (4.13) are the orthonormality conditions [22].

Expansion Theorem

The expansion theorem allows the admissible displacements to be represented as a linear combination of the eigenfunctions

$$Y(x) = \sum_{r=1}^{\infty} c_r Y_r(x) \tag{4.14}$$

where

$$c_r = m \int_0^1 Y_r(x) Y(x) dx \tag{4.15}$$

and

$$w_r^2 c_r = mEI \int_0^1 Y_r(x) \frac{d^4 Y(x)}{x^4} dx. \tag{4.16}$$

A solution to Eq. (4.8) is assumed to have the form $Y(x,t) = \sum_{r=1}^{\infty} Y_r(x)\eta(t)$. Equation (4.8) is multiplied by $Y_s(x)$ and integrated over the length of the beam to obtain

$$\begin{aligned} m \int_0^1 Y_s(x) Y_r(x) \frac{d^2 \eta_r(t)}{dt^2} dt = & - EI \int_0^1 Y_s(x) \eta_r(t) \frac{d^4 Y_r(x)}{dx^4} dx \\ & + \int_0^1 Y_s(x) F \delta(x-1) dx. \end{aligned} \tag{4.17}$$

Equations (4.12)-Eq. (4.13) are used to obtain the modal equation

$$\frac{d^2 \eta}{dt^2} + \omega_r \eta_r = \int_0^1 Y_r(x) F \delta(x-l) dx = Y_r(L) F. \tag{4.18}$$

The convolution integral is used to find the solutions of the modal Eq. (4.18)

$$\begin{aligned} \eta_r(t) &= \frac{Y_r(L)}{\omega_r} \int_0^1 F(t-\tau) \sin(\omega_r \tau) d\tau \\ &= \frac{Y_r(L)}{\omega_r} \int_0^1 F\mu(t-\tau) \sin(\omega_r \tau) d\tau \\ &= \frac{F_0 Y_r(L)}{\omega_r^2} (1 - \cos(\omega_r t)). \end{aligned} \tag{4.19}$$

so the displacement is

$$Y(x,t) = \sum_{r=1}^{\infty} Y_r(x)\eta_r(t) \approx \sum_{r=1}^{5} Y_r(x)\eta_r(t). \tag{4.20}$$

4.2.2 Comparison of Numeric and Modal Analysis

The numeric results are obtained by applying a step force to the cantilever tip in vacuum and recording the displacement of the tip. The computational effort is reduced by using the x-y plane of symmetry shown in Figure 4.4. The plane of symmetry is enforced by setting the z displacement equal to zero on the x-y plane. The cantilever is meshed with eight node rectangular prisms elements. The maximum side length of elements is $\max \Delta x = 1\,\mu\text{m}$.

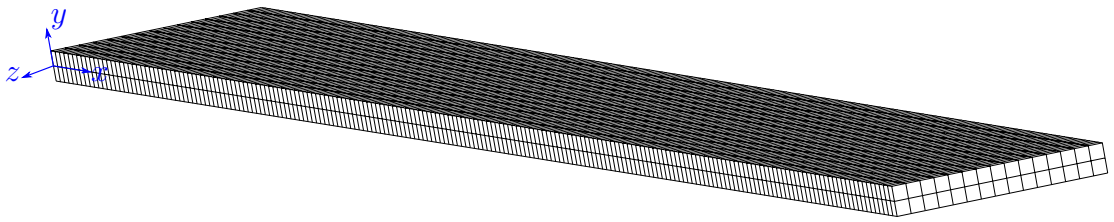

Figure 4.4: The mesh used to model the C2 cantilever for the validation testing. The x-y plane is used as a plane of symmetry and the beam is fixed on the y-z plane. A step force is applied to the cantilever tip in the positive y direction.

The tip displacement for the numeric and analytic solutions are compared in Figure 4.5.

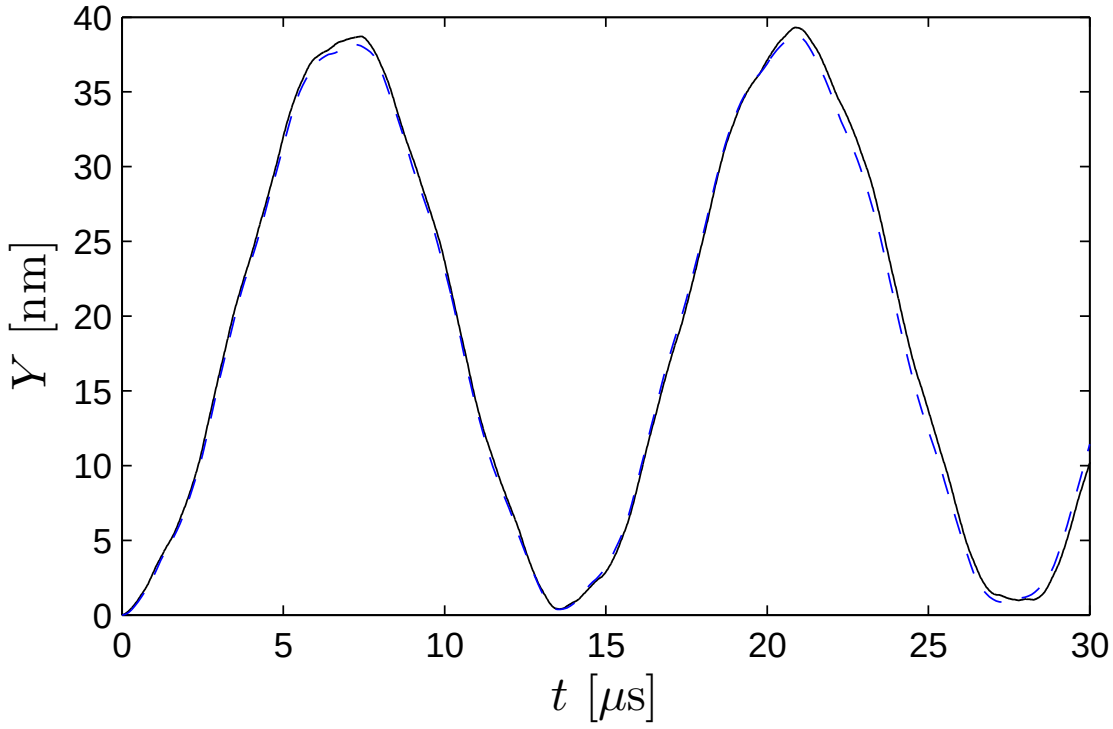

Figure 4.5: A comparison of the numeric and modal analysis solutions for the C2 cantilever. The solid line is the modal analysis solution and the dashed line is the numeric solution.

The error between the analytic and numeric solutions manifests itself mostly as a change in the frequency as displayed in Figure 4.5. The error in the numeric solution is quantified by the percent relative error between the numeric and analytic solutions.

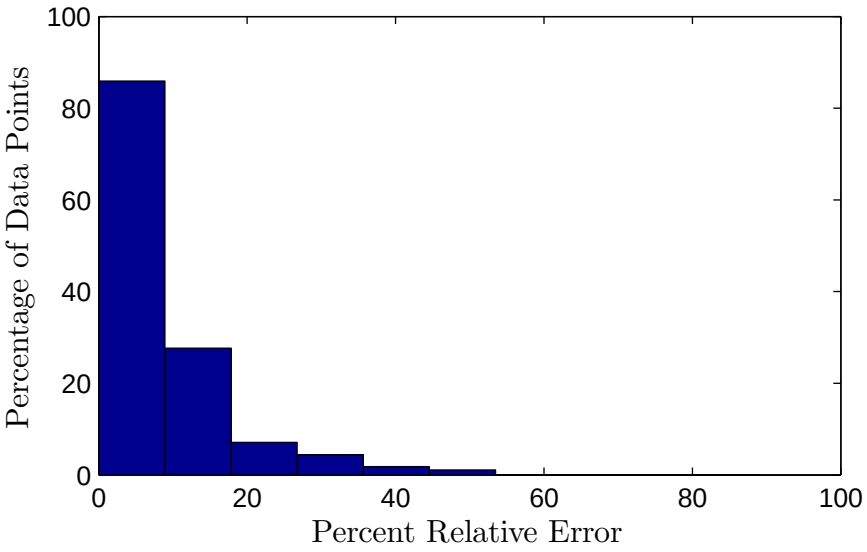

Figure 4.6: Histogram of the percent relative error between the numeric and analytic solutions of the C2 cantilever tip displacement. The numeric solution is found by finite element analysis and the analytic solution is found from modal analysis.

The percent relative error is less than 10% for the majority of the data points. The maximum percent relative error between the analytic and numeric solution is 89.1%. Low error between the numeric and analytic solutions in vacuum indicates that the solid model is a negligible source of error.

4.3 Validating the Fluid-solid Interaction

The C2 cantilever is now immersed in water and the fluid-solid interaction is solved. Noise spectrum and commonly used diagnostics, such as the quality factor Q of the C2 cantilever in water are determined. The numeric setup and procedure is validated by comparing the numeric noise spectrum and the analytic noise spectrum of Ref. [26].

The fluid-solid interaction combines the solid model of the C2 cantilever with a fluid model. The fluid model illustrated in Figure 4.7 is constructed by creating a box and subtracting the C2 cantilever from it using a Boolean operation. The solid walls that bound the fluid are separated from the C2 cantilever by $s_w = 20\,\mu\text{m}$. The x-y plane is used as a plane of symmetry by setting the z component of the velocity to zero on the x-y plane. The faces that coincide with the C2 cantilever are subdivided with $\min \Delta x = 1\,\mu\text{m}$ subdivisions, while the rest of the faces are subdivided with $\max \Delta x = 5\,\mu\text{m}$ subdivisions. A Delaunay meshing algorithm meshes the fluid domain with four node linear tetrahedral elements.

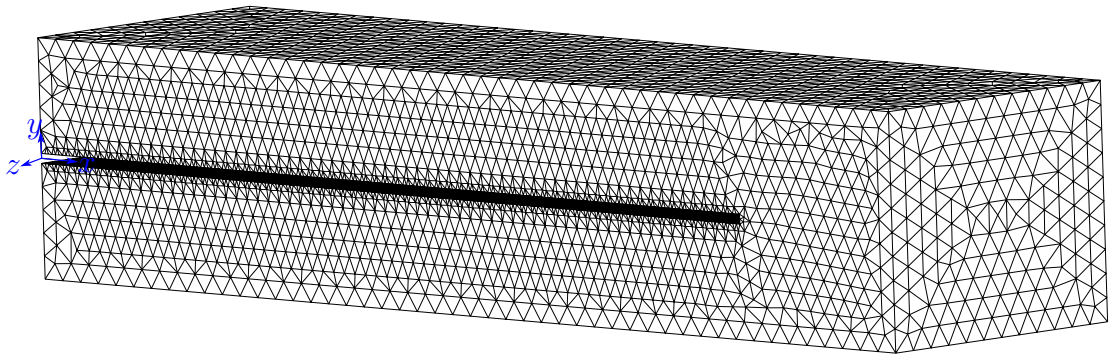

Figure 4.7: The fluid mesh used to model the water that immerses the C2 cantilever for the validation testing. The x-y plane is used as a plane of symmetry.

The solid model in Figure 4.4 and the fluid model in Figure 4.7 are loaded together and run with the a direct fluid-solid interaction coupling. The time step for the simulation is $\Delta t = 0.2\,\mu\text{s}$ and the tip displacement data is shown in Figure 4.8.

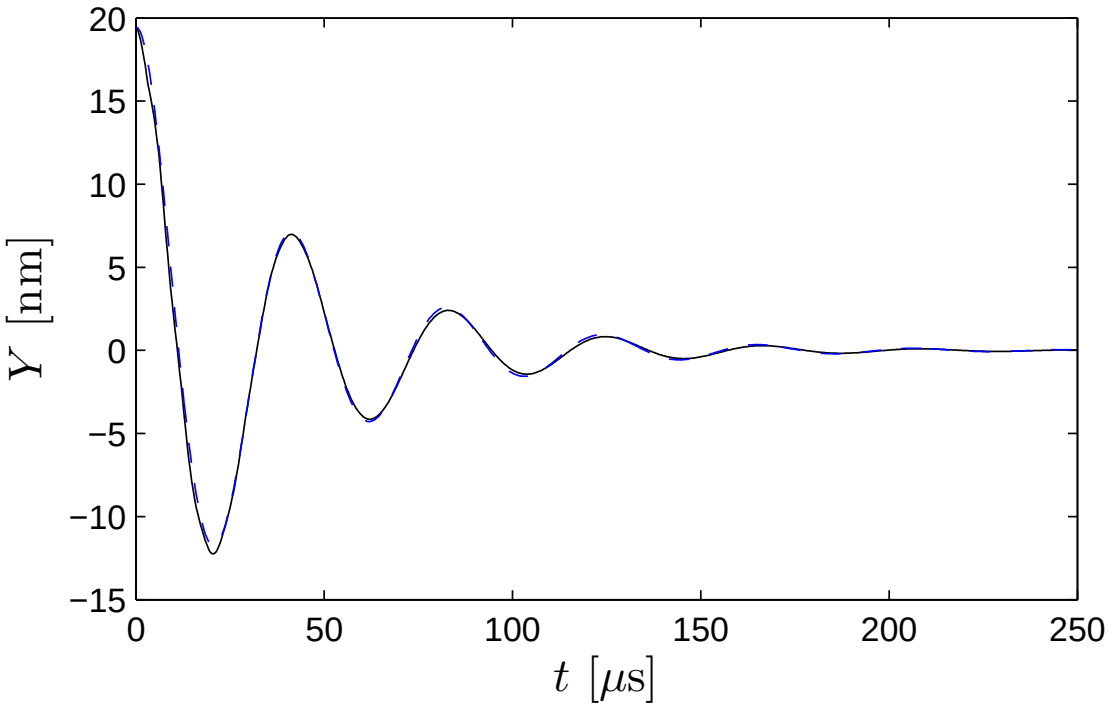

Figure 4.8: Tip displacement of the C2 cantilever in water released from a step force at $t = 0$ (solid line). A SHO is fitted to the tip displacement data (dashed line).

An underdamped simple harmonic oscillator (SHO) is fitted to the C2 tip displacement

data. The curve fit allows for commonly used diagnostics such as the quality factor Q and the fluid based frequency ω_f to be calculated. The motion of an underdamped SHO is valid for $Q > 1/2$ and is governed by

$$m_f \frac{d^2 Y_1(t)}{dt^2} + \gamma \frac{dY_1(t)}{dt} + kY_1(t) = 0, \tag{4.21}$$

where $Y_1(t)$ is the tip displacement of the underdamped SHO, m_f is the mass, γ is the damping, and k is the stiffness. The initial conditions are $Y_1(0) = F_0/k$ and $\frac{dY_1}{dt}|_{t=0} = 0$. The solution to Eq. (4.21) is

$$Y_1(t) = \frac{F_0}{k} e^{\frac{-\omega_f t}{2Q}} \left(\cos \omega_d t + \frac{\omega_f}{2Q\omega_d} \sin \omega_d t \right) \tag{4.22}$$

where

$$\omega_d = \omega_f \sqrt{1 - \frac{1}{4Q^2}}, \tag{4.23}$$

$\omega_f = \sqrt{k/m_f}$, and $Q_f = m\omega_0/\gamma$. A nonlinear least squares curve fit is used to fit Eq. (4.22) to the tip displacement of the C2 cantilever. The curve fit yields the values for Q, ω_f, γ_f, and m_f provided in Table 4.3. The curve fit displayed in Figure 4.8 is nearly indistinguishable from the numerics.

	Q	ω_f/ω_0	m_f/m_0
Analytic	3.24	0.34	8.16
Numeric	3.15	0.34	8.62

Table 4.3: The dynamics of the C2 cantilever calculated using the theory of Ref. [26] and the thermodynamic approach. m_f is the effective mass of the fundamental mode in water and $m_0 = 0.243\rho whL$ is the effective mass of the fundamental mode in vacuum [22].

The numerically calculated noise spectrum is compared with the analytic noise spectrum of the fundamental mode. The analytic noise spectrum for a long and thin cantilever is [26]

$$G(\omega) = \frac{4k_B T}{k\omega_0} \frac{T_0 \tilde{\omega} \Gamma_i \left(R_0 \tilde{\omega} \right)}{\left(1 - \tilde{\omega}^2 \left(1 + T_0 \Gamma_r \left(R_0 \tilde{\omega} \right) \right) \right)^2 + \left(\tilde{\omega}^2 + T_0 \Gamma_i \left(R_0 \tilde{\omega} \right) \right)^2} \tag{4.24}$$

where $\tilde{\omega} = \omega/\omega_0$, Γ_r is the real part of Γ, Γ_i is the imaginary part of Γ, R_0 is the frequency parameter, or frequency based Reynolds number evaluated at the natural frequency, and T_0 is the mass loading parameter [14]. The frequency parameter is

$$R_0 = \frac{\omega_0 w^2}{4\nu_f}. \tag{4.25}$$

The mass loading parameter, which is the ratio of the mass a cylinder of fluid with a radius $w/2$ to the actual mass of the cantilever, is given by

$$T_0 = \frac{\pi}{4}\frac{\rho_f w}{\rho_s h}. \tag{4.26}$$

Γ is the hydrodynamic function for a circular cylinder [2, 14]

$$\Gamma(\omega) = 1 + \frac{4iK_1(-i\sqrt{iR_0\tilde{\omega}})}{\sqrt{iR_0\tilde{\omega}}K_0(-i\sqrt{iR_0\tilde{\omega}})} \tag{4.27}$$

where $i = \sqrt{-1}$, $\tilde{\omega} = \omega/\omega_0$, and K_0 and K_1 are Bessel functions.

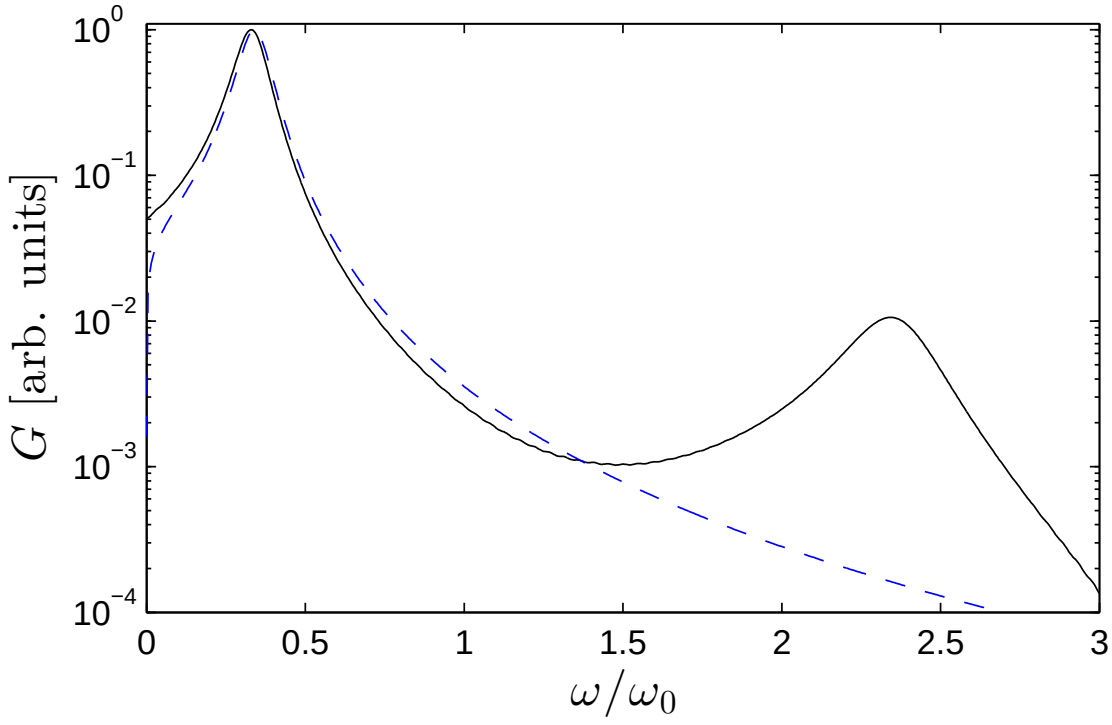

Figure 4.9: The noise spectrum G for the C2 cantilever in water. Two peaks of the numeric noise spectrum (solid black line) are displayed. The analytic noise spectrum of the fundamental mode (dashed blue line) matches numeric noise spectrum of the fundamental mode.

The good agreement between the numeric and analytic noise spectrum validates the numerical setup and procedure in fluid.

Chapter 5

Results

The properties of the nanobeam are dependent on the fluid in which it is immersed. The properties of the nanobeam are first determined in vacuum. Then the nanobeam is immersed in water and in air to determine how the properties of the nanobeam change with the fluid.

5.1 Nanobeam Properties

The material properties, stiffness, and natural frequency in vacuum are presented in Table 5.1.

E [GPa]	ρ_s [kg/m^3]	k [N/m]	f_0 [MHz]
174	2320	2.15	7.81

Table 5.1: The material properties, the stiffness k in the y direction, and the resonant frequency in vacuum f_0 of the nanobeam.

The stiffness of the nanobeam in the y direction is determined in Section 5.1.1 and the natural frequency of the nanobeam in vacuum is determined in Section 5.1.3.

5.1.1 Beam Stiffness

The stiffness measures how sensitive the nanobeam is to applied forces. Figure 3.2 illustrates the numerical setup used to determine the stiffness. The numerical analysis consists of applying a constant force to the nanobeam's tip in the y direction. Then the static tip

displacement Y_0 yields the stiffness of the nanobeam

$$k = \frac{F_0}{Y_0} = \frac{45\,\text{nN}}{20.9\,\text{nm}} = 2.15\,\text{N/m}. \tag{5.1}$$

The stiffness is easily tailored by altering the lengths $L1$ and $L2$ illustrated in Figure 3.4.

5.1.2 Stress distribution and Model for Stiffness

A constant force is applied to the tip of the nanobeam and the effective stress of the nanobeam is plotted in Figure 5.1. The effective stress plot shows that most of the strain is experienced by the support beams. The middle potion of the beam that wraps around the microdisk experiences small and nearly uniform strain.

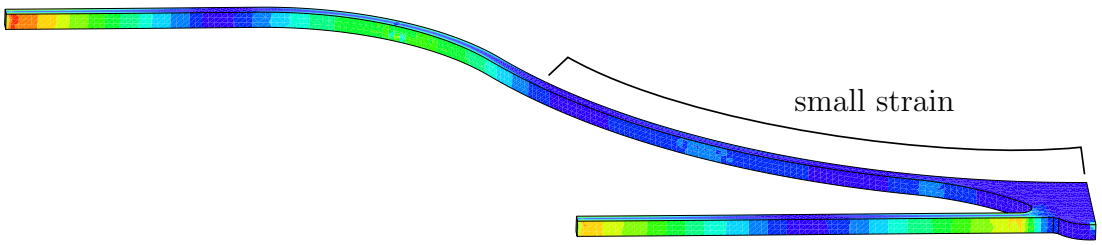

Figure 5.1: An effective stress plot of the nanobeam with a constant force applied to the tip. The stress in the nanobeam is 105 MPa (red), 60 MPa (green), and 15 MPa (blue). A large portion of the nanobeam that wraps around the microdisk experiences small strain and stress.

The stress plot indicates that a simple model may be able to predict the stiffness of the nanobeam. The effective stress plots of the front and back support beams resemble those of a doubly clamped beam. Two doubly clamped beams that are connected in series are used to model the nanobeam. This model is depicted in Figure 5.2.

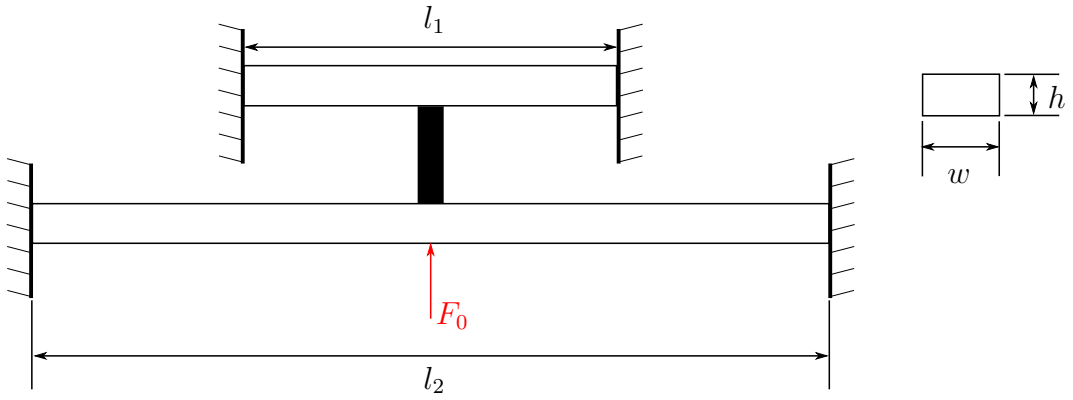

Figure 5.2: A model to predict the stiffness on the nanobeam. l_1 is the effective length of the front supports of the nanobeam and l_2 is the effective length of the back supports

The stiffness of a doubly clamped beam k_{dcb} subjected to a force at its midspan is [22]

$$k_{\text{dcb}} = 192\frac{EI}{L^3} \tag{5.2}$$

where L is the length of the beam. The effective length of the front beam is $l_2 = L_2 - 1.2\,\mu\text{m} = 7\,\mu\text{m}$ where $1.2\,\mu\text{m}$ is the width of the intersection of the nanobeam's tip and the front beam. The effective length of the back beam is $l_1 = L_1 - 2(r_1 + r_2) = 2.2\,\mu\text{m}$. Using the effective lengths of the front and back beam the stiffness of the nanobeam is estimated

$$k = \left(\frac{1}{k_{\text{dcb},1}} + \frac{1}{k_{\text{dcb},2}}\right)^{-1} = \left(\frac{1}{71} + \frac{1}{2.1}\right)^{-1} = 2.1\,\text{N/m}. \tag{5.3}$$

The error between the stiffness given by the double clamped beam model and the stiffness given from the finite element analysis is less than three percent.

5.1.3 Natural Frequency

A larger natural frequency of the nanobeam corresponds to a faster acquisition rate. A faster acquisition rate means more data can be collected in a shorter amount of time and interactions that occur on smaller timescales can be resolved. Numerical modal analysis determines the natural frequency of the nanobeam in vacuum. The fundamental mode illustrated in Figure 5.3 is in plane with the microdisk and has a natural frequency of $f_0 = 7.81\,\text{MHz}$.

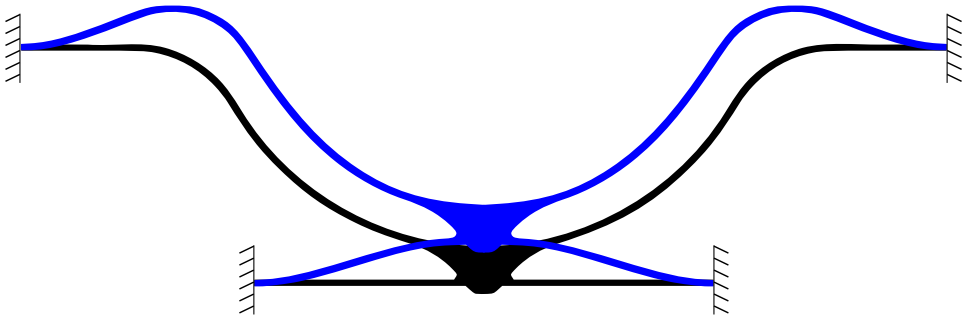

Figure 5.3: The fundamental mode of the nanobeam (blue) in vacuum is in plane with the microdisk optical resonator. The undeformed position (black) is shown. The fundamental frequency is $f_0 = 7.81\,\mathrm{MHz}$.

5.2 Nanobeam in Water

Because many biological and chemical applications of AFM occur in water, we now determine the nanobeam properties in water. Water with a density of $\rho_f = 997\,\mathrm{kg/m^3}$ and a dynamic viscosity $\mu_f = 8.59 \times 10^{-4}\,\mathrm{Pa\,s}$ immerses the nanobeam. The nanobeam frequency parameter, mass loading parameter, Stokes length, and Knudsen number are provided in Table 5.2. The mean free path λ of the water is not defined because the water molecules are in constant contact with one another [33]. Therefore, the diameter of a water molecule $\lambda = 0.3\,\mathrm{nm}$ is used to calculate the Knudsen number.

R_0	T_0	δ_0 [nm]	Kn
0.963	0.878	132	0.001

Table 5.2: The frequency parameter based on the vacuum resonant frequency R_0, the mass loading factor T_0, the Stokes length δ_0 in water based on the natural frequency, and the Knudsen number Kn in water. The fluid is water with $\rho_f = 997\,\mathrm{kg/m^3}$ and $\mu_f = 8.59 \times 10^{-4}\,\mathrm{Pa\,s}$.

Figure 3.2 illustrates the numerical setup used to determine the nanobeam's properties in water. The nanobeam wraps around the microdisk as illustrated in Figure 3.1. The microdisk is expected to significantly affect the nanobeam dynamics because of its close proximity to the nanobeam. The gap between the nanobeam and the microdisk resonator is $s_g = 100\,\mathrm{nm} \approx 0.76\delta_0$. A step force is applied to the tip of the nanobeam in the distant past and released at $t = 0$. The tip displacement recorded in Figure 5.4 illustrates that the nanobeam is overdamped in water. An overdamped SHO is fitted to the nanobeam's tip displacement data. The motion of an overdamped SHO is valid for $Q < 1/2$. The motion of

the overdamped SHO released from an initial displacement Y_0 is [26]

$$Y_2(t) = Y_0 \left(\frac{\lambda_2}{\lambda_2 - \lambda_1} e^{\lambda_1 t} + \frac{\lambda_1}{\lambda_1 - \lambda_2} e^{\lambda_2 t} \right) \tag{5.4}$$

where

$$\lambda_{1,2} = \omega_f \left(-\frac{1}{2Q} \pm \sqrt{\frac{1}{4Q^2} - 1} \right). \tag{5.5}$$

Y_2 is the displacement of the overdamped SHO. The sum of the squared errors measures how well the curve fit matches the data

$$S_E = \sum_{i=1}^{n} (Y_i - Y_{2,i})^2 \tag{5.6}$$

where n is the number of data observations, Y_i are the numerical results, and $Y_{2,i}$ are results from the curve fit. $S_E = 131\,\mathrm{nm}^2$ for the non-linear least squares regression fit of Eq. (5.4) to the displacement data given in Figure 5.4. The nanobeam is overdamped and has a quality factor $Q \ll 1/2$.

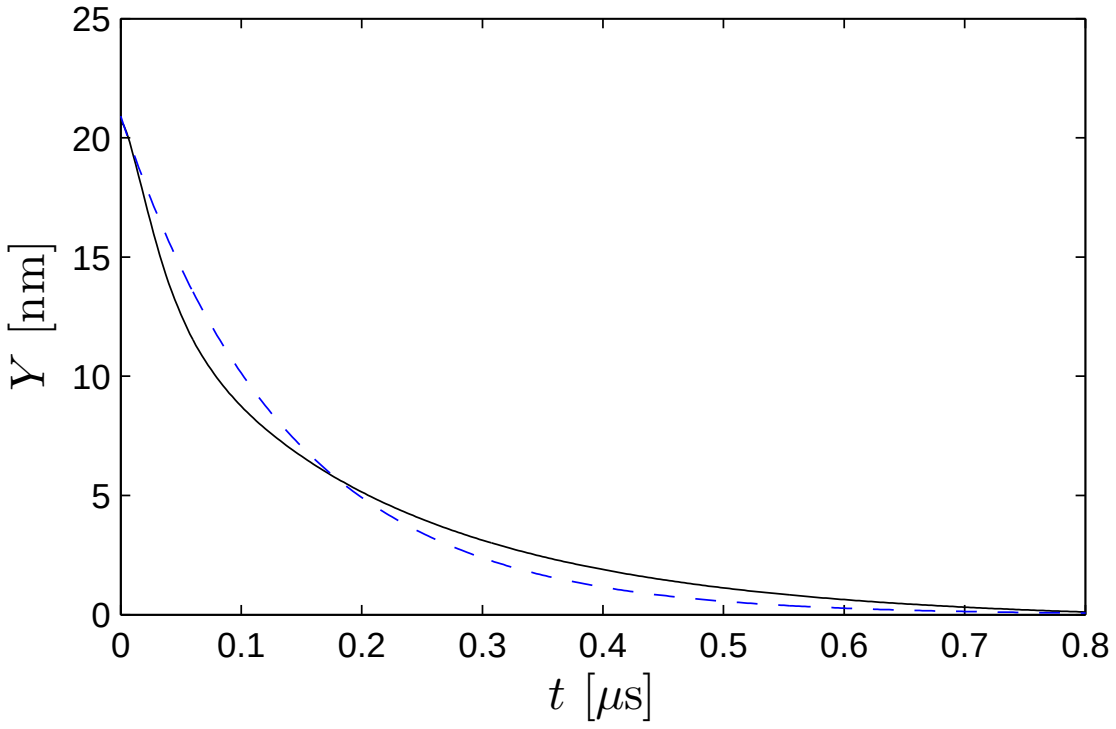

Figure 5.4: Tip displacement of the nanobeam Y released from a step force at $t = 0$ (solid black line) and the overdamped SHO curve fit (blue dashed line). The nanobeam is in close proximity to the microdisk and is immersed in water.

The autocorrelation of the nanobeam's tip displacement fluctuations from equilibrium is given in Figure 5.5 and is found using Eq. 2.10.

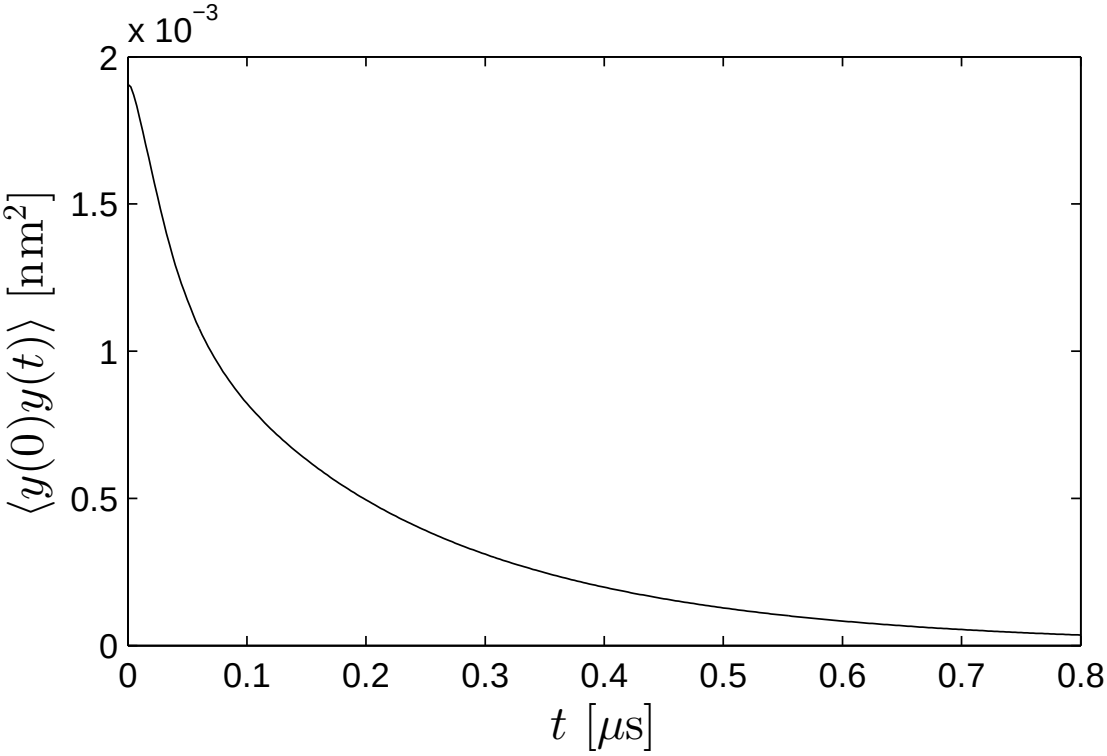

Figure 5.5: The autocorrelation of the nanobeam's tip displacement fluctuations from equilibrium. The nanobeam is in close proximity to the microdisk and is immersed in water.

The noise spectrum G given in Figure 5.6 is found using Eq. (2.9).

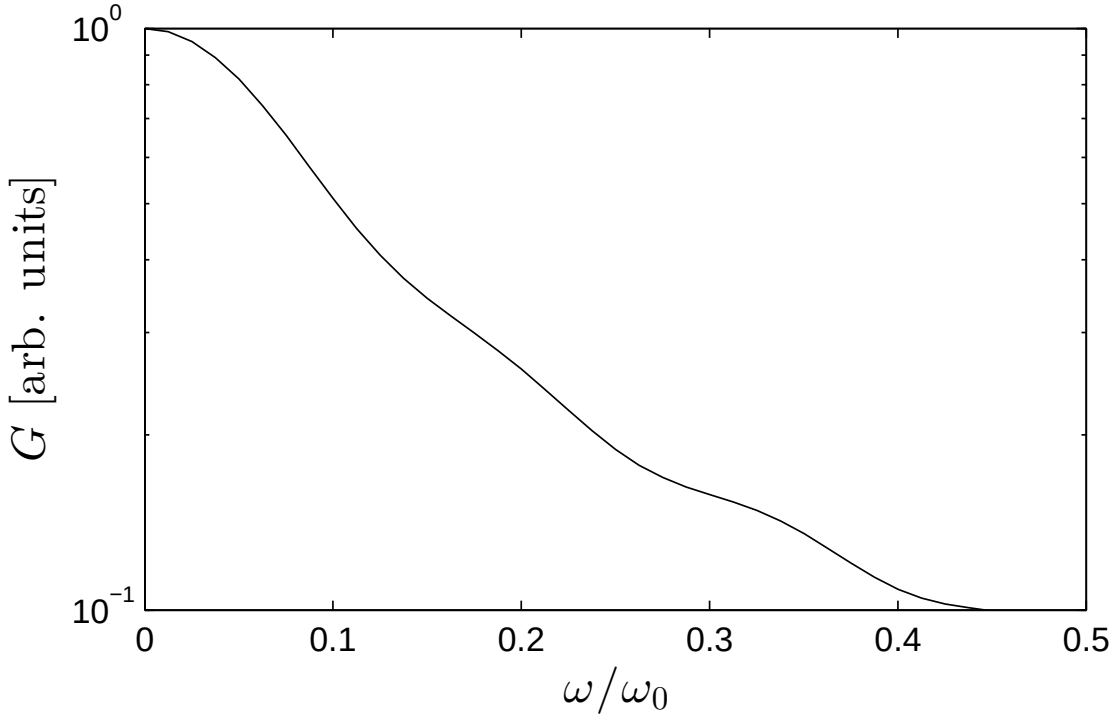

Figure 5.6: The noise spectrum G of the nanobeam's tip displacement fluctuations from equilibrium. The amplitude of the noise spectrum is normalized so the maximum value is unity. The microdisk is included and the nanobeam is immersed in water.

The maximum amplitude of the noise spectrum is achieved when $\omega/\omega_0 = 0$.

5.2.1 Omitting the Microdisk

Omitting the microdisk demonstrates how the small gap s_g between the nanobeam and the microdisk increases the damping of the nanobeam. An underdamped SHO is fitted to the nanobeam's tip displacement data given in Figure 5.7. The curve fit is governed by Eq. (4.21) and the solution is given by Eq. (4.22). The logarithmic decrement method is used to fit the SHO to the data. The logarithmic decrement method is useful when the assumption that the damping is proportional to the velocity is only approximately true [22]. $S_E = 85.7\,\mathrm{nm}^2$ for the SHO curve fit using the logarithmic decrement method. In contrast, a non-linear least squares regression fit produces a $S_E = 1370\,\mathrm{nm}^2$ when the initial guesses are the output of the logarithmic decrement method. The tip displacement data and the curve fit are given in Figure 5.7. The quality factor and natural frequency of the nanobeam in water are provided in Table 5.3.

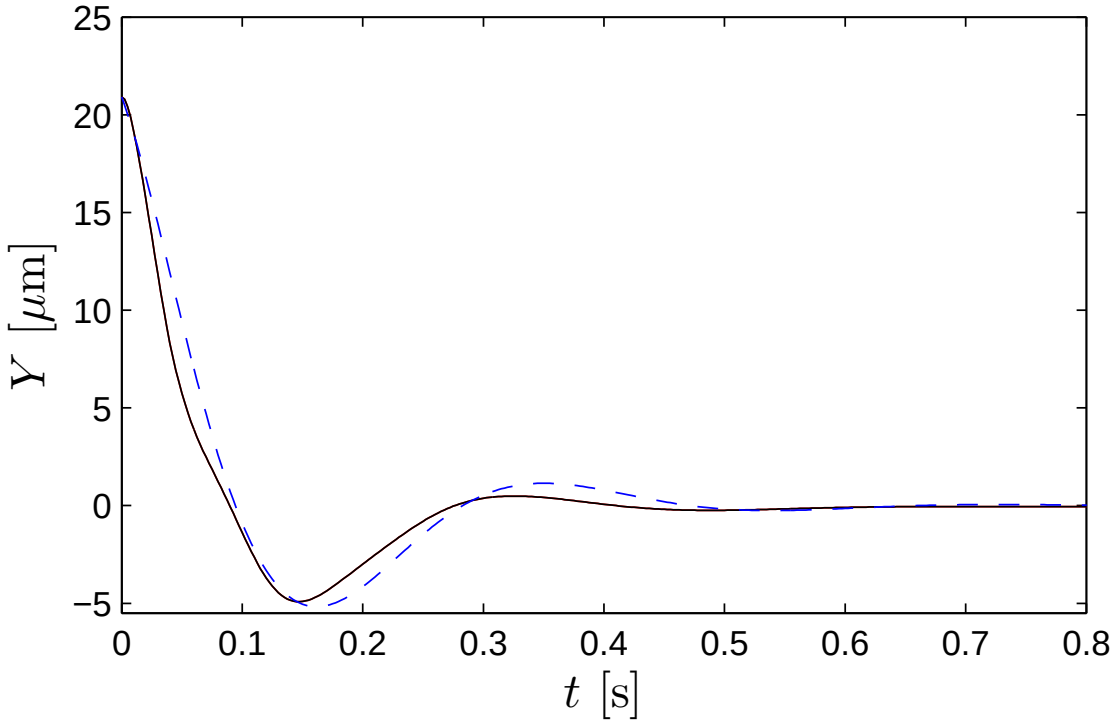

Figure 5.7: Tip displacement of the nanobeam Y released from a step force at $t = 0$ (solid black line) and the underdamped SHO curve fit (blue dashed line). The nanobeam is immersed in water and the microdisk is omitted.

Q	ω_f/ω_0	m_f/m_0
1.6	0.38	5.8

Table 5.3: A simple harmonic oscillator is fit to the displacement data to determine the quality factor in water Q, the natural frequency in water ω_f, and the effective mass of the fundamental mode m_f in water. $m_0 = k/\omega_0^2$ is the effective mass of the fundamental mode in vacuum. The nanobeam is immersed in water and the microdisk is omitted.

The autocorrelation of the nanobeam's tip displacement fluctuations from equilibrium is given in Figure 5.8.

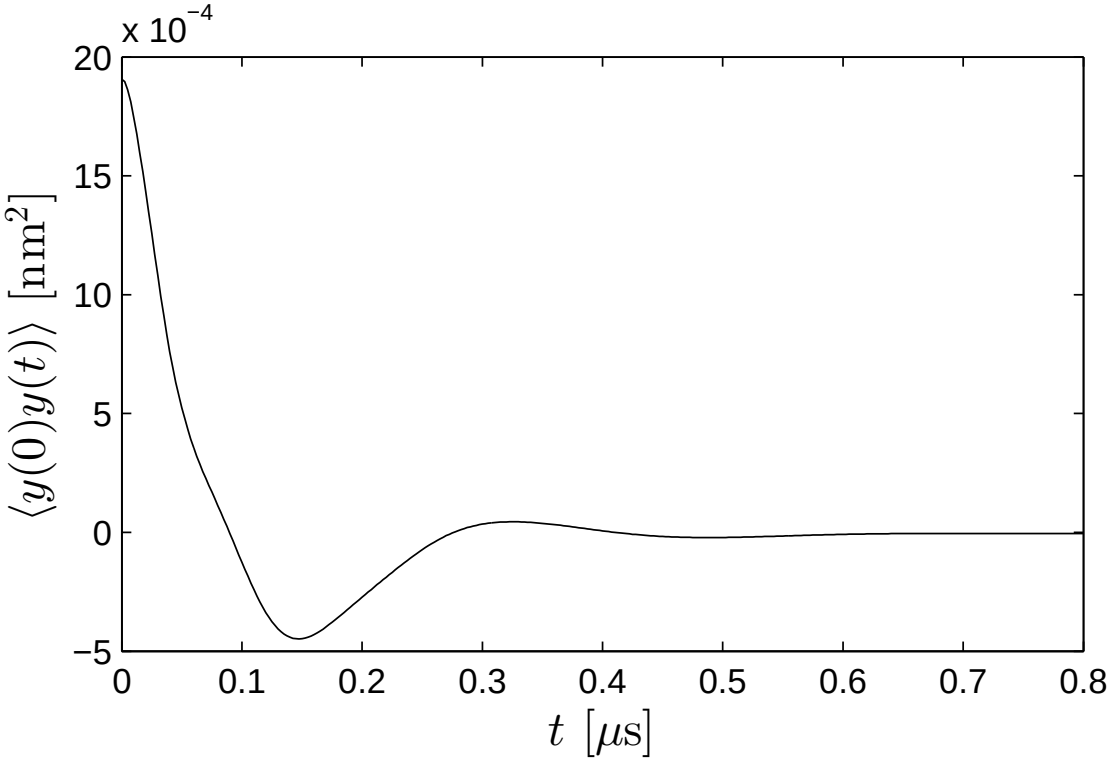

Figure 5.8: The autocorrelation of the nanobeam's tip displacement fluctuations from equilibrium. The nanobeam is immersed in water and the microdisk is omitted.

The noise spectrum G is given in Figure 5.9.

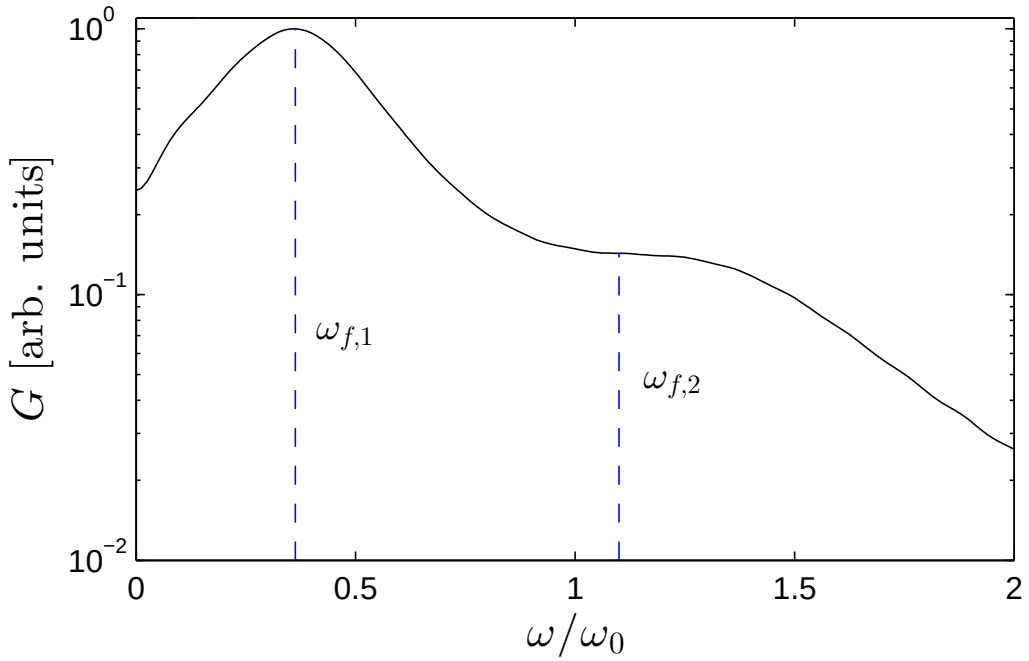

Figure 5.9: The noise spectrum G of the nanobeam's tip displacement fluctuations from equilibrium. The amplitude of the noise spectrum is normalized so the maximum value is unity. Two modes ($\omega_{f,1}$ and $\omega_{f,2}$) are clearly seen. The nanobeam is immersed in water and the microdisk is omitted.

The maximum amplitude of the noise spectrum is achieved when $\omega/\omega_0 = 0.363$. Two peaks are clearly seen in the noise spectrum. The peaks in the noise spectrum are quite close together.

5.2.2 Analytic Noise Spectrum of the Nanobeam

The analytic noise spectrum of the nanobeam in water with the microdisk omitted is given in Figure 5.10. The analytic noise spectrum peaks at a lower frequency than the numeric noise spectrum. Also the analytic quality factor is smaller than the numeric quality factor. The two quality factors are compared in Table 5.4.

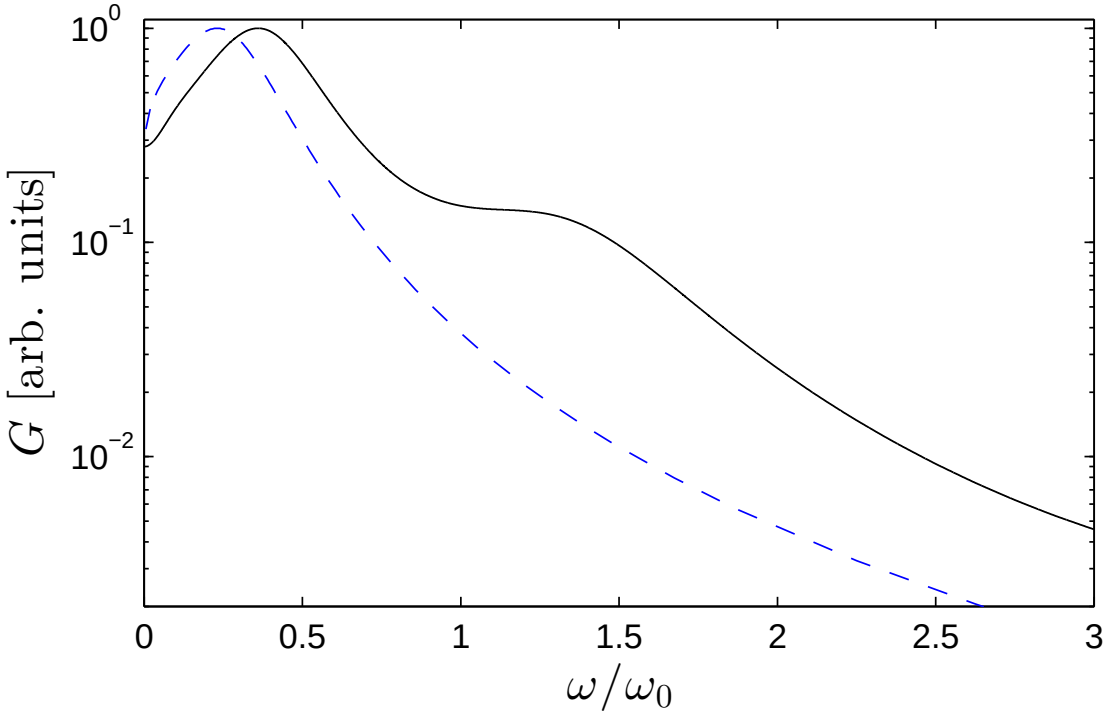

Figure 5.10: A comparison of the numeric (black solid line) and the analytic (dashed blue line) noise spectrum of the nanobeam in water. The microdisk is omitted and the amplitude is normalized so the maximum value of G is unity.

	numeric	analytic
Q	1.6	1.1

Table 5.4: The numeric and analytic quality factor Q of the nanobeam in water when the microdisk is omitted.

5.3 Nanobeam in Air

The dynamics of the nanobeam in air are now explored. The density of the air is $\rho_f = 1.275\,\mathrm{kg/m^3}$ and the dynamic viscosity is $\mu_f = 1.9 \times 10^{-5}\,\mathrm{Pa\,s}$. The air can be treated as a continuum because the Knudsen number

$$\mathrm{Kn} = \frac{\lambda}{w} = \frac{70\,\mathrm{nm}}{260\,\mathrm{nm}} = 0.27 \tag{5.7}$$

is less than 0.3, $\mathrm{Kn} < 0.3$ [33]. The properties of the nanobeam in air are provided in Table 5.5.

R_0	T_0	δ_0 [nm]	Kn
0.056	0.0011	551	0.27

Table 5.5: Frequency parameter based on the vacuum resonant frequency R_0, the mass loading factor T_0 and the Stokes length δ_0 in air based on the natural frequency in vacuum ω_0. The fluid is air with $\rho_f = 1.275\,\mathrm{kg/m^3}$ and $\mu_f = 1.9 \times 10^{-5}\,\mathrm{Pa\,s}$.

An underdamped SHO is fitted to the nanobeam's tip displacement data in air. A non-linear least squares regression fit of Eq. (4.21) to the displacement data provided in Figure 5.11 produces of $S_E = 180\,\mathrm{nm^2}$.

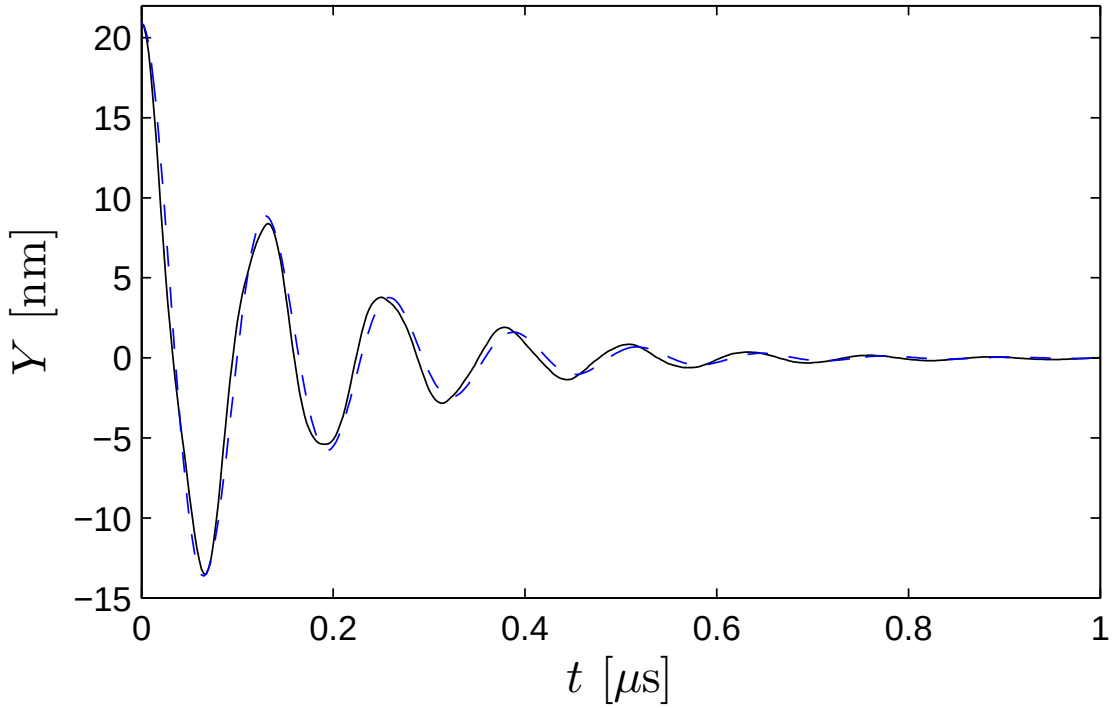

Figure 5.11: Tip displacement of the nanobeam in air released from a step force at $t = 0$ (solid black line). A SHO is fitted to the tip displacement data (dashed blue line). The microdisk is included.

Commonly used diagnostics of the nanobeam in air are provided in Table 5.6.

Q	ω_f/ω_0	m_f/m_0
4.16	≈ 1	≈ 1

Table 5.6: A simple harmonic oscillator is fit to the data to determine the quality factor Q, the natural frequency in air ω_f, and the effective mass of the fundamental mode in air m_f. $m_0 = k/\omega_0^2$ is the effective mass of the fundamental mode in vacuum.

The autocorrelation of the spontaneous fluctuations from equilibrium are given in Figure 5.12.

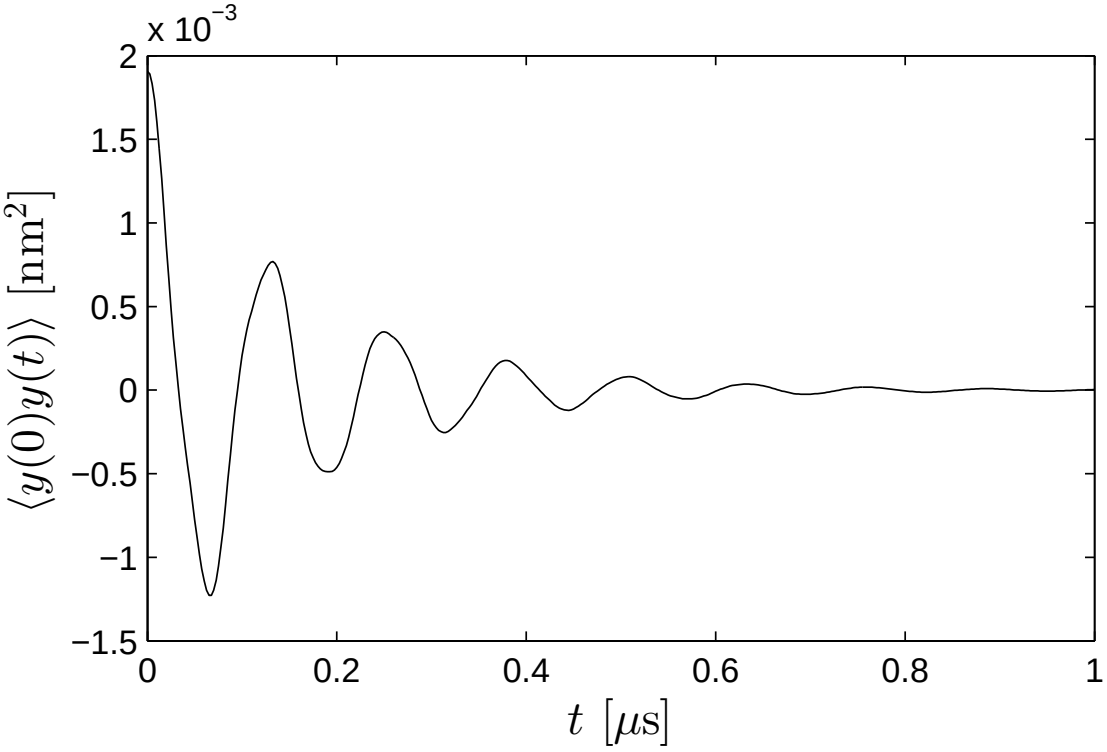

Figure 5.12: The autocorrelation of the nanobeam's tip displacement fluctuations from equilibrium. The nanobeam is immersed in air and the microdisk is included.

The noise spectrum is given in Figure 5.13.

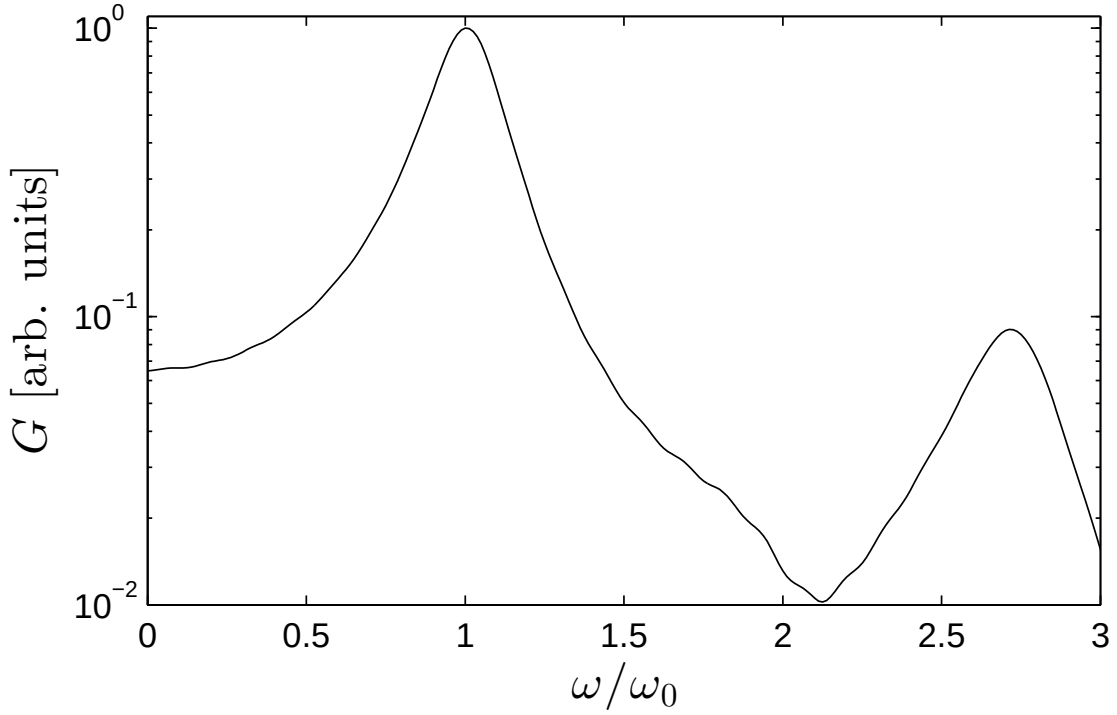

Figure 5.13: The noise spectrum G of the nanobeam's tip displacement fluctuations from equilibrium. The amplitude is normalized so the maximum value of G is unity. Two modes ($\omega_{f,1}$ and $\omega_{f,2}$) are clearly seen. The nanobeam is immersed in air and the microdisk is included.

The maximum amplitude of the noise spectrum is achieved when $\omega/\omega_0 \approx 1$. Two peaks are clearly seen in the noise spectrum.

5.3.1 Omitting the Microdisk

Omitting the microdisk demonstrates how the small gap $s_g = 100\,\text{nm}$ between the nanobeam and the microdisk increases the damping of the nanobeam in air. An underdamped SHO is fitted to the nanobeam's tip displacement data given in Figure 5.14. The curve fit is governed by Eq. (4.21) and the solution is given by Eq. (4.22). The logarithmic decrement method is used to fit the SHO to the data. The tip displacement data and the curve fit are given in Figure 5.14. The quality factor and natural frequency of the nanobeam in air are provided in Table 5.7.

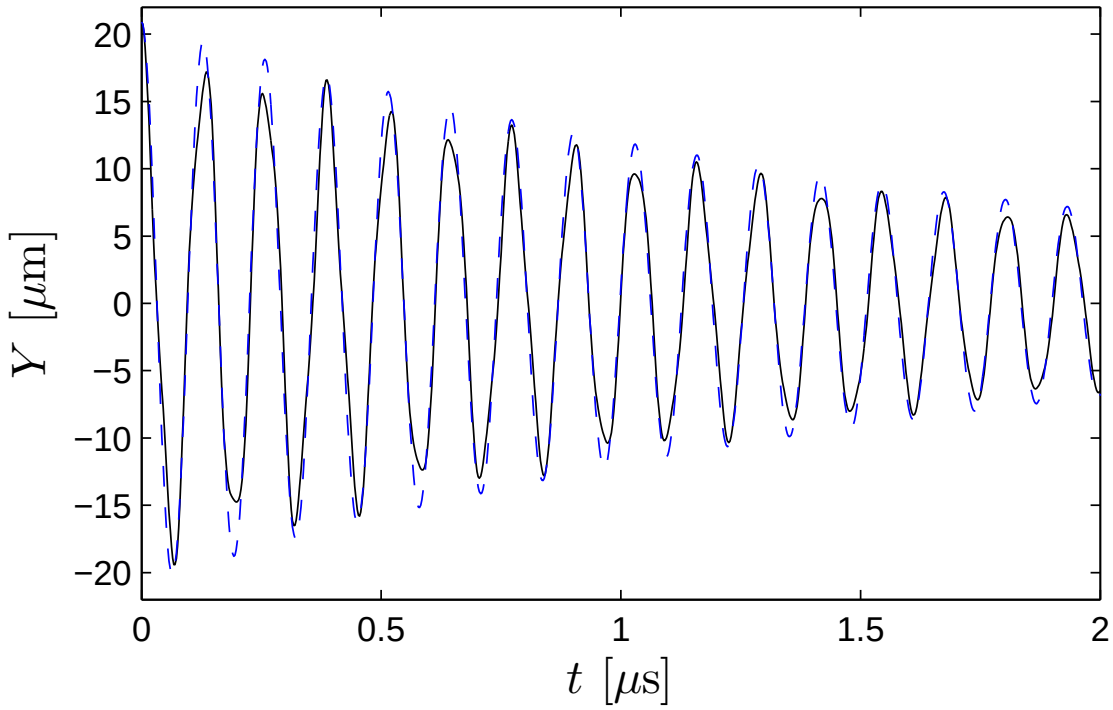

Figure 5.14: Tip displacement of the nanobeam Y released from a step force at $t = 0$ (solid black line) and the underdamped SHO curve fit (blue dashed line). The nanobeam is immersed in air and the microdisk is omitted.

Q	ω_f/ω_0	m_f/m_0
44	≈ 1	≈ 1

Table 5.7: A simple harmonic oscillator is fit to the displacement data to determine the quality factor in air Q, the natural frequency in air ω_f, and the effective mass of the fundamental mode m_f in air. The nanobeam is immersed in air and the microdisk is omitted.

The autocorrelation of the nanobeam's tip displacement fluctuations from equilibrium is given in Figure 5.15.

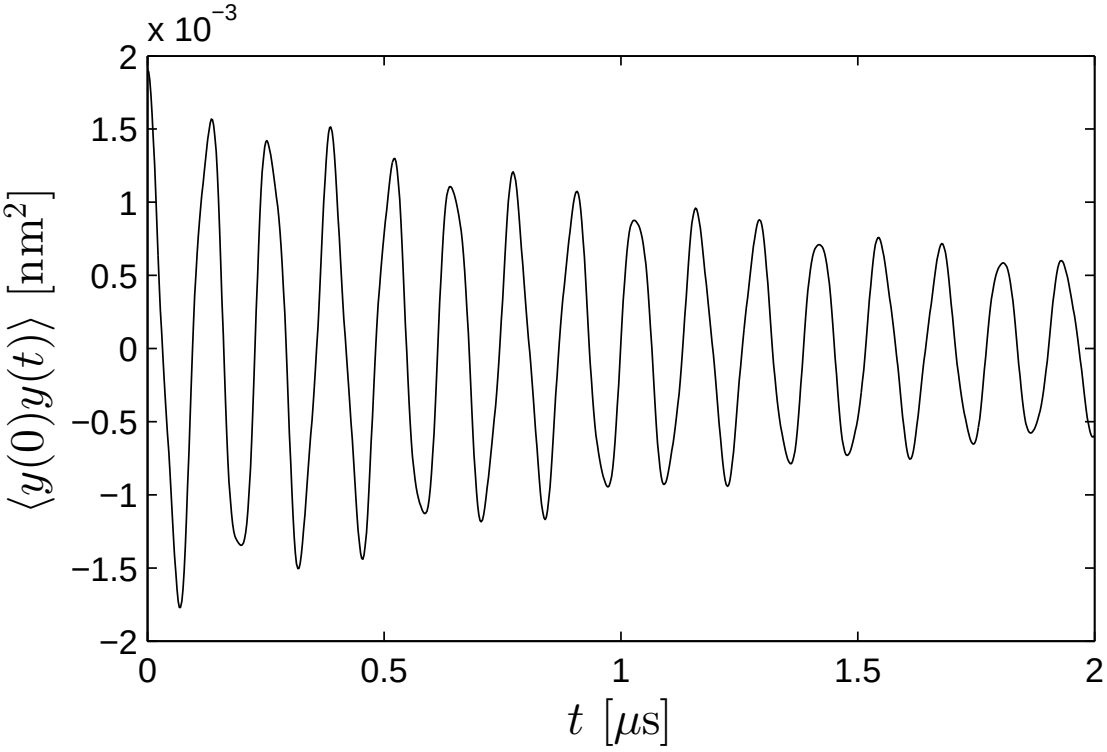

Figure 5.15: The autocorrelation of the nanobeam's tip displacement fluctuations from equilibrium. The nanobeam is immersed in air and the microdisk is omitted.

The noise spectrum is given in Figure 5.16.

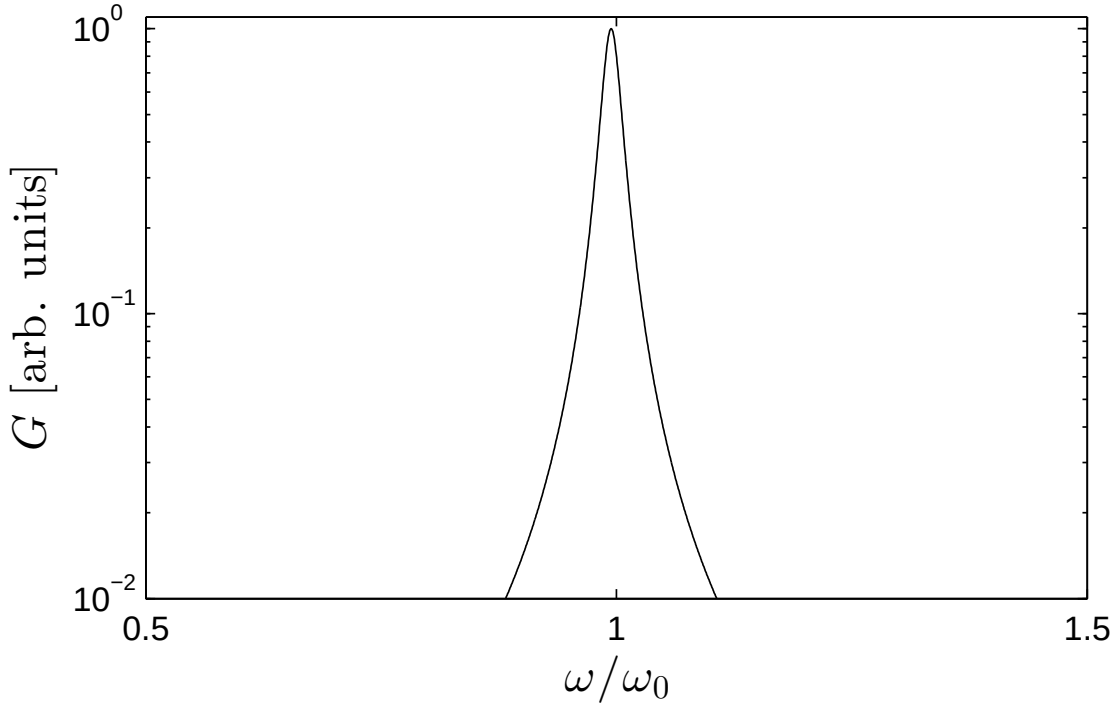

Figure 5.16: The noise spectrum G of the nanobeam's tip displacement fluctuations from equilibrium. The amplitude of the noise spectrum is normalized so the maximum value is unity. Two modes ($\omega_{f,1}$ and $\omega_{f,2}$) are clearly seen. The nanobeam is immersed in air and the microdisk is omitted.

The maximum amplitude of the noise spectrum is achieved when $\omega/\omega_0 \approx 1$. Two peaks are clearly seen in the noise spectrum. The peaks in the noise spectrum are quite close together.

5.3.2 Analytic Noise Spectrum of the Nanobeam

The analytic noise spectrum of the nanobeam in air shows good agreement with the numeric noise spectrum when the microdisk is omitted. The analytic noise spectrum is given in Figure 5.17. The numeric and analytic quality factors are compared in Table 5.8.

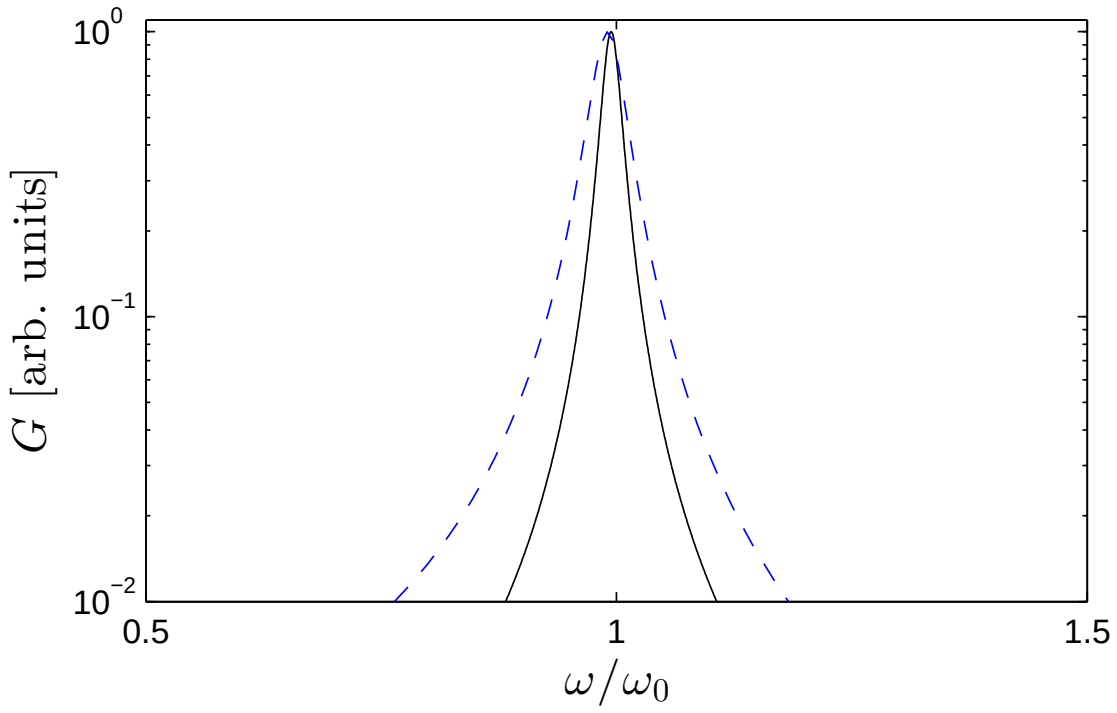

Figure 5.17: A comparison of the numeric (solid black line) and analytic noise spectrum (dashed blue line) of the nanobeam in air. The microdisk is omitted and the amplitude is normalized so the maximum value of G is unity.

	numeric	analytic
Q	44	24

Table 5.8: The numeric and analytic quality factor Q of the nanobeam in air when the microdisk is omitted.

5.4 Peak Separation and Quality Factor

The separation between the first and second modes and the quality factor of the first mode of the nanobeam are provided in Table 5.9. The peak separation in air is nearly the same as the peak separation in vacuum. However, the peak separation in water is larger than the peak separation in vacuum.

	ω_1/ω_0	ω_2/ω_0	ω_2/ω_1	Q
vacuum	1	2.7	2.7	NA
water (microdisk)	NA	NA	NA	$\ll 0.5$
water (no microdisk)	0.36	1.15	3.2	1.6
air (microdisk)	≈ 1	≈ 1	2.7	4.16
air (no microdisk)	≈ 1	≈ 2.7	2.7	44

Table 5.9: The first peak of the nanobeam's noise spectrum at the frequencies ω_1 and the second peak is at ω_2. Q is the quality factor of the first mode. The modes reported are in-plane with the microdisk and symmetric about the y-z plane.

Chapter 6

Conclusion

A thermodynamic approach is used to determine the stochastic dynamics of a nanobeam used in cavity optomechanical sensors for AFM, which are immersed in a viscous fluid. In order to use a thermodynamic approach the major sources of dissipation must be accurately modeled. Viscous dissipation is the major source of dissipation of energy from the nanobeam. The viscous damping is increased by the small gap, $s_g = 100\,\text{nm}$, between the nanobeam and the microdisk. The increase in viscous damping caused by s_g is demonstrated by the results of nanobeam in water. The nanobeam is underdamped when the microdisk is omitted, but is overdamped when the microdisk is included. In air, despite the inclusion of the microdisk, the nanobeam is underdamped.

The viscous dissipation is determined from finite element simulations that must accurately model the interaction between the nanobeam and the fluid that immerses the nanobeam. This interaction is found to be accurately modeled by available commercial finite element software. The ADINA® direct fluid-solid interaction capabilities produce results in agreement with theory for a cantilever in water. Because analytic results do not exist for a curved nanobeam, the numeric results for the nanobeam are validated by testing to make sure the results are independent of the computational parameters. Mesh independence, domain independence, and time step independence studies are performed to ensure the results of the nanobeam are independent of the computation parameter.

Over a dozen simulations are required to perform the three tests for computational parameter independence. Each simulation can take can take months to complete. Fortunately, the time to complete the simulations is reduced from months to weeks by using two planes of symmetry.

The thermodynamic approach can produce results for complicated geometry, such as the curved nanobeam, in a timely manner. The results for the quality factor, the natural frequency in fluid, and noise spectrum found for the nanobeam in water and in air will prove usefully for experimentalist and designers of cavity optomechanical sensors for AFM.

Bibliography

[1] Atomic force microscope - park systems AFM,Research,Industrial.

[2] *Laminar boundary layers: an account of the development, structure, and stability of laminar boundary layers in incompressible fluids, together with a description of the associated experimental techniques*. Dover Publications, New York, 1988.

[3] ADINA system online manuals, 2011.

[4] T. Albrecht and C. Quate. Atomic resolution imaging of a nonconductor by atomic force microscopy. *Journal of Applied Physics*, 62(7):2599–2602, October 1987.

[5] G. Anetsberger, O. Arcizet, Q. Unterreithmeier, R. Rivière, A. Schliesser, E. Weig, J. Kotthaus, and T. Kippenberg. Near-field cavity optomechanics with nanomechanical oscillators. *Nature Physics*, 5(12):909–914, December 2009.

[6] G. Bao and S. Suresh. Cell and molecular mechanics of biological materials. *Nature Materials*, 2(11):715–725, November 2003.

[7] S. Basak, A. Raman, and S. Garimella. Hydrodynamic loading of microcantilevers vibrating in viscous fluids. *Journal of Applied Physics*, 99(11):114906–114906–10, June 2006.

[8] K. Bathe. *Finite Element Procedures*. Klaus-Jurgen Bathe, February 2007.

[9] K. Bathe and H. Zhang. A mesh adaptivity procedure for CFD and fluid-structure interactions. *Computers & Structures*, 87(11–12):604–617, June 2009.

[10] D. Chandler. *Introduction to Modern Statistical Mechanics*. Oxford University Press, USA, 1 edition, September 1987.

[11] C. Chatfield. *The Analysis of Time Series: An Introduction, Sixth Edition*. Chapman and Hall/CRC, 6 edition, July 2003.

[12] J. Chon, P. Mulvaney, and J. Sader. Experimental validation of theoretical models for the frequency response of atomic force microscope cantilever beams immersed in fluids. *Journal of Applied Physics*, 87(8):3978–3988, April 2000.

[13] M. Clark and M. Paul. The stochastic dynamics of rectangular and v-shaped atomic force microscope cantilevers in a viscous fluid and near a solid boundary. *Journal of Applied Physics*, 103(9):094910–094910–9, May 2008.

[14] M. Clark, J. Sader, J. Cleveland, and M. Paul. Spectral properties of microcantilevers in viscous fluid. *Physical Review E*, 81(4):046306, April 2010.

[15] C. Green and J. Sader. Small amplitude oscillations of a thin beam immersed in a viscous fluid near a solid surface. *Physics of Fluids*, 17(7):073102–073102–12, July 2005.

[16] H. Haus. *Waves and Fields in Optoelectronics*. Prentice Hall, September 1983.

[17] M. Hopcroft, W. Nix, and T. Kenny. What is the Young's modulus of silicon? *Journal of Microelectromechanical Systems*, 19(2):229 –238, April 2010.

[18] T. Ikehara, J. Lu, M. Konno, R. Maeda, and T. Mihara. A high quality-factor silicon cantilever for a low detection-limit resonant mass sensor operated in air. *Journal of Micromechanics and Microengineering*, 17(12):2491, December 2007.

[19] T. Kippenberg and K. Vahala. Cavity opto-mechanics. *Optics Express*, 15(25):17172–17205, December 2007.

[20] Y. Liu, H. Miao, V. Aksyuk, and K. Srinivasan. Wide stiffness range cavity optomechanical sensors for atomic force microscopy. In *Integrated Photonics Research, Silicon and Nanophotonics*, OSA Technical Digest (online), page IW2C.5. Optical Society of America, June 2012.

[21] J. Lübbe, L. Tröger, S. Torbrügge, R. Bechstein, C. Richter, A. Kühnle, and M. Reichling. Achieving high effective Q-factors in ultra-high vacuum dynamic force microscopy. *Measurement Science and Technology*, 21(12):125501, December 2010.

[22] L. Meirovitch. *Fundamentals of Vibrations*. Waveland Pr Inc., 1 edition, July 2010.

[23] H. Miao, K. Srinivasan, and V. Aksyuk. A microelectromechanically controlled cavity optomechanical sensing system. *New Journal of Physics*, 14(7):075015, July 2012.

[24] R. Pathria. *Statistical Mechanics, Second Edition*. Butterworth-Heinemann, 2 edition, August 1996.

[25] M. Paul, M. Clark, and M. Cross. The stochastic dynamics of micron and nanoscale elastic cantilevers in fluid: fluctuations from dissipation. *Nanotechnology*, 17(17):4502–4513, September 2006.

[26] M. Paul and M. Cross. Stochastic dynamics of nanoscale mechanical oscillators immersed in a viscous fluid. *Physical Review Letters*, 92(23):235501, June 2004.

[27] A. Raman, J. Melcher, and R. Tung. Cantilever dynamics in atomic force microscopy. *Nano Today*, 3(1–2):20–27, February 2008.

[28] Lord Rayleigh. *The Theory of Sound, Volume 2*. Dover, second revised edition, January 1945.

[29] J. Reddy. *An Introduction to the Finite Element Method*. McGraw-Hill Science/Engineering/Math, 3 edition, January 2005.

[30] J. Sader. Frequency response of cantilever beams immersed in viscous fluids with applications to the atomic force microscope. *Journal of Applied Physics*, 84(1):64–76, July 1998.

[31] J. Sader, J. Chon, and P. Mulvaney. Calibration of rectangular atomic force microscope cantilevers. *Review of Scientific Instruments*, 70(10):3967–3969, October 1999.

[32] H. Schlichting and K. Gersten. *Boundary-Layer Theory*. Springer, 8th edition, March 2000.

[33] T. Squires and S. Quake. Microfluidics: Fluid physics at the nanoliter scale. *Reviews of Modern Physics*, 77(3):977–1026, October 2005.

[34] K. Srinivasan, H. Miao, M. Rakher, M. Davanço, and V. Aksyuk. Optomechanical transduction of an integrated silicon cantilever probe using a microdisk resonator. *Nano Letters*, 11(2):791–797, February 2011.

[35] K. Vahala. Optical microcavities. *Nature*, 424(6950):839–846, August 2003.

[36] S. Verbridge, L. Bellan, J. Parpia, and H. Craighead. Optically driven resonance of nanoscale flexural oscillators in liquid. *Nano Letters*, 6(9):2109–2114, September 2006.

[37] M. Viani, L. Pietrasanta, J. Thompson, A. Chand, I. Gebeshuber, J. Kindt, M. Richter, H. Hansma, and P. Hansma. Probing protein-protein interactions in real time. *Nature structural biology*, 7(8):644–647, August 2000. PMID: 10932247.

[38] M. Viani, T. Schäffer, A. Chand, M. Rief, H. Gaub, and P. Hansma. Small cantilevers for force spectroscopy of single molecules. *Journal of Applied Physics*, 86(4):2258–2262, August 1999.

[39] M. Villa and M. Paul. Stochastic dynamics of micron-scale doubly clamped beams in a viscous fluid. *Physical Review E*, 79(5):056314, May 2009.